SPECIAL
Climate and Frontal Air-Sea Interaction
COLLECTION

Distinct Influence of Air–Sea Interactions Mediated by Mesoscale Sea Surface Temperature and Surface Current in the Arabian Sea

HYODAE SEO

Physical Oceanography Department, Woods Hole Oceanographic Institution, Woods Hole, Massachusetts

ABSTRACT

During the southwest monsoons, the Arabian Sea (AS) develops highly energetic mesoscale variability associated with the Somali Current (SC), Great Whirl (GW), and cold filaments (CF). The resultant high-amplitude anomalies and gradients of sea surface temperature (SST) and surface currents modify the wind stress, triggering the so-called mesoscale coupled feedbacks. This study uses a high-resolution regional coupled model with a novel coupling procedure that separates spatial scales of the air–sea coupling to show that SST and surface currents are coupled to the atmosphere at distinct spatial scales, exerting distinct dynamic influences. The effect of mesoscale SST–wind interaction is manifested most strongly in wind work and Ekman pumping over the GW, primarily affecting the position of GW and the separation latitude of the SC. If this effect is suppressed, enhanced wind work and a weakened Ekman pumping dipole cause the GW to extend northeastward, delaying the SC separation by 1°. Current–wind interaction, in contrast, is related to the amount of wind energy input. When it is suppressed, especially as a result of background-scale currents, depth-integrated kinetic energy, both the mean and eddy, is significantly enhanced. Ekman pumping velocity over the GW is overly negative because of a lack of vorticity that offsets the wind stress curl, further invigorating the GW. Moreover, significant changes in time-mean SST and evaporation are generated in response to the current–wind interaction, accompanied by a noticeable southward shift in the Findlater Jet. The significant increase in moisture transport in the central AS implies that air–sea interaction mediated by the surface current is a potentially important process for simulation and prediction of the monsoon rainfall.

1. Introduction

The western Arabian Sea (AS) experiences the seasonally reversing monsoonal winds, which drive energetic spatiotemporal variability related to the Somali Current, Great Whirl, and cold filaments. The Somali Current (SC) is a powerful western boundary current in the Indian Ocean, whose northeastward surface current speeds during the summer monsoon reach up to $2–3\,\mathrm{m\,s^{-1}}$ (Swallow and Bruce 1966; Swallow et al. 1983; Beal and Donohue 2013). The SC separates from the Somali Coast at about 10°N, hugging the northern shoulder of the Great Whirl (Swallow and Bruce 1966) and feeding into the Southwest Monsoon Current. Earlier studies suggest that the SC becomes unstable, leading to enhanced instabilities and nonlinearity (Cox 1979; Kindle and Thompson 1989; McCreary et al. 1993; Wirth et al. 2002; Jochum and Murtugudde 2005).

The Great Whirl (GW), a large (a diameter of ~300 km), semipermanent anticyclonic eddy, is the most striking mesoscale circulation feature in the Indian Ocean during the summer monsoon (Schott and McCreary 2001). Many previous studies have examined mechanisms for formation and maintenance of the GW. Some point to local wind curl east of the Findlater (or Somali) Jet (Leetmaa et al. 1982; Luther and O'Brien 1989), while others attribute the formation and maintenance to the remote influence of the westward-propagating Rossby waves (Schott and Quadfasel 1982; Brandt et al. 2003; Beal and Donohue 2013). Jensen (1991) suggests that large kinetic energy of the SC and lateral gradient in relative vorticity lead to barotropic instability and formation of the GW. Once formed, the GW exhibits chaotic and anisotropic variability (Beal and Donohue 2013), often moving its position by 2° latitude within a short period of time. The GW is mostly flanked by the cyclones to the north and east. Baroclinic instability resulting from the interaction

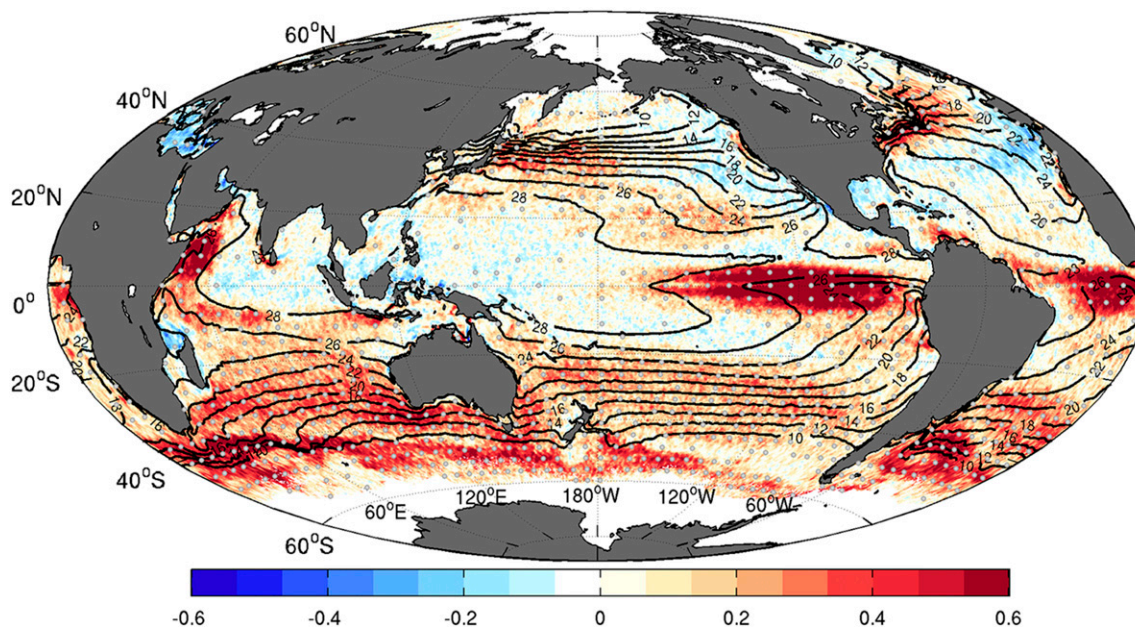*Corresponding author*: Hyodae Seo, hseo@whoi.edu

FIG. 1. Map of correlation between the daily zonally highpass-filtered (10° longitudes) SST and WS for the boreal summer (June–September) of 2001–09. The SST is based on the NOAA Objectively Interpolated SST (AVHRR-only; Reynolds et al. 2007), and WS is based on the QuikSCAT data, both on 0.25° by 0.25° grid. The black contours denote the climatological JJAS SST [contour interval (CI) = 2°C]. Gray dots, plotted every 6° longitudes and 4° latitudes, denote the significant correlation at the 95% confidence level.

of the GW with these adjacent cyclones is suggested as a principal mechanism for the decay of the GW (Jensen 1993). To the north of the GW at 9°–11°N is found the wedgelike cold filament (CF), which is a primary pathway of upwelled water to spread offshore in the form of a zonal jet (Schott 1983; Fischer et al. 2002). The GW often blocks the SC and deflects it into this strong offshore zonal jet.

Sea surface temperature (SST) difference between the GW and the CF greatly exceeds 5°C (Vecchi et al. 2004). Complex mesoscale flows also produce large surface vorticity leading to a Rossby number near unity (Vic et al. 2014). These large-amplitude SST and current velocity/vorticity fields modify wind stress, wind stress curl, and Ekman pumping velocity, which can influence the dynamics of the AS circulation (Vecchi et al. 2004) as well as the space–time structure of the Findlater Jet (Mafimbo and Reason 2010). This feedback can be particularly important for the Indian summer monsoon, given the strong statistical correlation among the western AS SST, the Findlater Jet, and the summer monsoon rainfall over India (Shukla 1975; Murtugudde and Busalacchi 1999; Izumo et al. 2008). Yet, few systematic studies exist to elucidate the dynamics and impacts of mesoscale air–sea interactions in the AS. In particular, it is unknown if and how current–wind coupling affects the AS circulation and what its relative role is in comparison to SST–wind coupling.

Some satellite-based studies have documented significant wind response to mesoscale SSTs in the AS (Vecchi et al. 2004) and over the global oceans [see Small et al. (2008) for a review]. Figure 1 shows a global map of correlation between daily wind speed (WS) and daily SST during the boreal summer [June–September (JJAS)] of 2001–09. The WS and SST are zonally highpass filtered (10°) to remove large-scale air–sea coupling (which is generally negative, not shown). It is evident that the correlation is positive over most of the global oceans, especially where the eddy activity is significant, such as the eastern equatorial Pacific and Atlantic Oceans and western boundary currents in the midlatitudes. Note that the western AS supports the strongest mesoscale SST–wind coupling in the Indian Ocean, indicating a significant mesoscale SST–wind covariability takes place in association with the SC, GW, and CF. The positive correlation reflects the active role that mesoscale SSTs play in the atmospheric boundary layer dynamics (Wallace et al. 1989). That is, reduced vertical shear over warmer SST (e.g., GW) facilitates turbulent mixing of momentum between the lower- and upper-level winds, accelerating surface wind and wind stress. The opposite applies to cold SST (e.g., CF), where stable stratification decouples the wind near the surface from that aloft, causing the surface wind to slow down by friction.

In addition, Chelton et al. (2004) found that the SST gradients almost instantaneously modify the wind stress

curl and Ekman pumping (W_e). This SST-induced W_e persists on a time scale of $O(1)$ month with an average amplitude of $1\,\mathrm{m\,day}^{-1}$, which led Vecchi et al. (2004) to hypothesize that this anomaly should be important for the observed thermocline variability. Seo et al. (2008) support this hypothesis by showing that W_e over the CF is comparable to total vertical velocity associated with baroclinic instability near the CF. This suggests that the SST-induced W_e should be as important as the internal ocean dynamics for the evolution of CF. Recent modeling studies have begun to recognize the importance of mesoscale SST–wind interaction. Hogg et al. (2009) note the strong destabilizing effect by the SST-driven W_e on the modeled double-gyre circulation, particularly in the western boundary, where the intergyre potential vorticity flux weakens the flow through the instability of the eastward jet. Similarly, Ma et al. (2016) document that mesoscale SST–wind interaction leads to a substantial dissipation of eddy potential energy over the Kuroshio, thereby weakening its eastward jet. However, the extent to which it affects the SC, the western boundary current of the AS, is unknown. This is the first goal of the study.

Additionally, recent regional coupled modeling studies by Seo et al. (2016) and Renault et al. (2016a) have suggested the importance of current–wind interaction for the energetics of the California Current System [see also Renault et al. (2016b) for the Gulf Stream]. The bulk aerodynamic formula for wind stress is expressed as

$$\boldsymbol{\tau} = \rho_a C_D (\mathbf{u}_a - \mathbf{u}_o) |\mathbf{u}_a - \mathbf{u}_o|, \tag{1}$$

where $\boldsymbol{\tau}$ is the wind stress, ρ_a the density of the air, C_D the drag coefficient, and $\mathbf{u}_a$ and $\mathbf{u}_o$ the wind velocity and the ocean surface current velocity, respectively. Since the strong surface current with large vorticity evolves under the steady Findlater Jet, the AS currents are expected to modify the wind stress by creating velocity shear across the air–sea interface and through the vorticity of surface flow (McGillicuddy et al. 2007; Mahadevan et al. 2008; Gaube et al. 2015). The influence of current–wind interaction has been examined in a number of numerical modeling studies over different parts of the world's oceans (e.g., Pacanowski 1987; Duhaut and Straub 2006; Seo et al. 2007b; Zhai and Greatbatch 2007; Small et al. 2009; Eden and Dietze 2009; Hutchinson et al. 2010). These studies suggest that the inclusion of surface current in the bulk formula reduces the strength of mesoscale eddy activity and large-scale currents by enhancing surface drags, diminishing wind work, and modifying Ekman pumping. The second goal of the study is, therefore, to examine the dynamical response of the AS circulation to air–sea coupling through surface currents.

Because of their uncoupled nature, many ocean modeling studies mentioned above fail to capture simultaneous effects of SST- and current-driven air–sea interactions. These studies also cannot investigate rectified atmospheric response. The downstream development of the Findlater Jet is particularly sensitive to slight variations in SST and evaporation over the western AS because of the highly nonlinear nature of the jet (Krishnamurti and Bhalme 1976). The change in the Findlater Jet is important for the monsoon, as its onset precedes that of the rainfall over India by several days, with the rainfall amount corresponding well to the jet intensity (Halpern and Woiceshyn 2001). To investigate the dynamical influence of the air–sea interactions mediated by mesoscale SST and surface currents on the AS circulation and the Findlater Jet, we use a high-resolution fully coupled regional climate model with a novel scale-selective air–sea coupling strategy. To the best of the author's knowledge, no coupled modeling studies exist for the AS that separate mesoscale air–sea interactions through SST and surface currents.

The paper is organized as follows. Section 2 describes the regional coupled model (2a) and experimental configurations (2b–d) and also introduces the online smoothing procedure (2e) and the observational datasets used in the study (2f). Section 3 first compares the simulated mean states to the observed estimates (3a), followed by the discussion on impacts of the mesoscale SST–wind (3b) and current–wind interaction (3c). Section 4 investigates causes of the response through the energetics analysis. Section 5 explores the time-mean responses in the Findlater jet and associated water vapor transport, followed by a summary and discussion in section 6.

2. Model, experiments, and data

a. Model description

The Scripps Coupled Ocean–Atmosphere Regional (SCOAR) model (Seo et al. 2007a, 2014, 2016; http://hseo.whoi.edu/scoar) is a regional coupled climate model that couples the Weather Research and Forecast (WRF; Skamarock et al. 2008) Model to the Regional Ocean Modeling System (ROMS; Haidvogel et al. 2000; Shchepetkin and McWilliams 2005). The interacting boundary layer is based on the bulk formula (Fairall et al. 1996; 2003), which calculates the surface momentum, heat, and freshwater fluxes using near-surface meteorological fields from WRF and SST and surface currents from ROMS. The WRF and ROMS cover the identical AS domain (Fig. 3) both on 9-km grids with matching land–sea mask. ROMS (WRF) is run with 30 vertical levels, with 10 layers in the upper 150 m (below 750 m) to capture the surface boundary layer processes
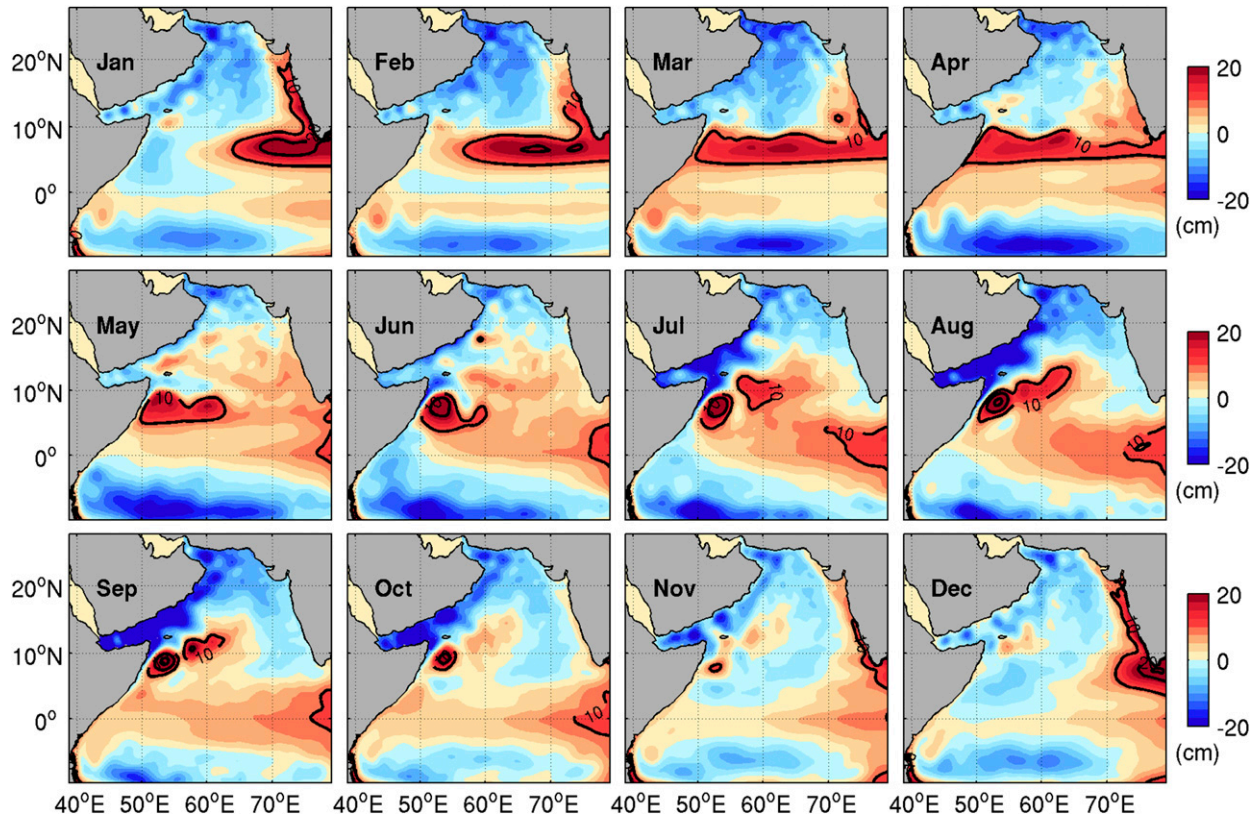
FIG. 2. Monthly evolution of SSHA (cm) from the 10-yr ROMS spinup simulation.

(e.g., O'Neill et al. 2010). The model coupling is activated every 6 h to account for the diurnal cycle.

b. Model physics

WRF uses the modified Tiedtke cumulus parameterization scheme, including CAPE-removal time scale, shallow component, and momentum transport (Tiedtke 1989; Zhang et al. 2011). The cloud microphysics is represented by the WRF single-moment 6-class scheme (Hong and Lim 2006) and the planetary boundary layer by the Yonsei University (YSU) nonlocal scheme (Hong et al. 2006). The Rapid Radiative Transfer Model (RRTM; Mlawer et al. 1997) and the Goddard scheme (Chou and Suarez 1999) are used for longwave and shortwave radiation transfer. The land surface process is treated with the Noah land surface model (Chen and Dudhia 2001). In ROMS, the mixed layer processes are parameterized using a K-profile parameterization (KPP) scheme (Large et al. 1994). No explicit horizontal diffusivity is used, although implicit numerical diffusivity is introduced by the advection scheme (Haidvogel et al. 2000).

c. Spinup simulation and internal variability

Before the WRF–ROMS coupled integrations, the 10-yr ROMS spinup simulation is driven by the climatological

monthly temperature and salinity (1980–2007) from the Simple Ocean Data Assimilation (SODA; Carton and Giese 2008) and the momentum, heat, and freshwater fluxes from the Comprehensive Ocean–Atmosphere Dataset (da Silva et al. 1994). Time series of the domain-averaged, depth-integrated kinetic energy (not shown) indicates that a quasi-steady state is reached by the third year (e.g., Vic et al. 2014). Figure 2 shows the monthly evolution of the 10-yr climatological sea surface height anomaly (SSHA). The well-known westward-propagating Rossby wave is apparent. The positive SSHA is radiated from the southern tip of India during the winter monsoon (December–January) and arrives in the Somali Coast by March–April in spring. With the summer monsoon onset (May–June), the GW develops in 4°–10°N accompanied by the wedgelike negative SSHA, or CF, over 9°–11°N (July–August). The GW and CF reach their peak intensity in June–August but begin to decay slowly toward the winter monsoon. The seasonal behavior of the basinwide SSHA variability is in reasonable agreement with the monthly composites presented by Beal and Donohue (2013).

d. Coupled model simulation

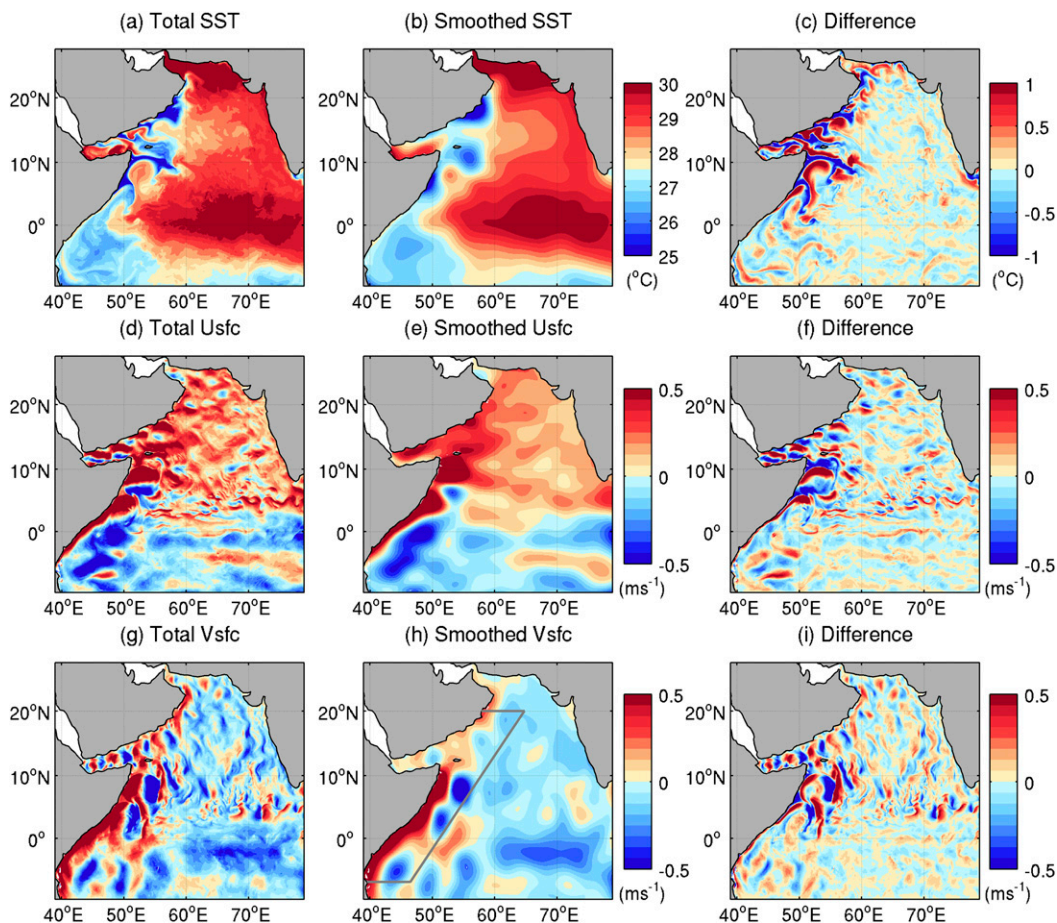The ocean state on 1 April from the 10th year of the spinup simulation is used as the ROMS initial condition

FIG. 3. Example of a 5° lowess filtering applied to the daily snapshot (1 Aug 2009) of the ocean surface fields, (a)–(c) SST (°C), (d)–(f) surface zonal current U_{sfc} (m s^{-1}), and (g)–(i) surface meridional current V_{sfc} (m s^{-1}). The fields (left) before and (center) after the smoothing; (right) the difference (before minus after). The gray box in (h) denotes the area in which the alongshore averages of the EKE budget terms are calculated for Figs. 8 and 9.

for WRF–ROMS coupled runs. For the lateral boundary condition for ROMS, the time-varying monthly SODA temperature and salinity fields are used. The WRF is initialized at 0000 UTC 1 April from the 1° National Centers for Environmental Prediction (NCEP) Operational Global Final Analyses (FNL). The 6-hourly FNL data are also used as lateral boundary conditions for WRF. The control simulation (CTL) is integrated for 6 months from 1 April to 30 September for 10 years (2001–10). The first two months (1 April to 31 May) are disregarded as a coupled boundary layer spinup. On 1 June in each of the 10 years, three sensitivity simulations, as described below, branch off from the CTL.

The CTL and three sensitivity simulations, identical except in the way the wind stress is calculated, are designed to isolate the influences of air–sea interaction arising from mesoscale SST and surface current. In CTL, full SST and surface currents from the 9-km ROMS are used for wind stress. In the noT$_e$ run, where the mesoscale SST (T_e)

effect on wind stress is suppressed, the ROMS SST is spatially smoothed before its use in the bulk formula (section 2e). Likewise, in the noU$_e$, the effect of eddy-induced surface current (U_e) on wind stress is removed by spatially smoothing surface currents. Note that background currents are still used in the bulk formula. An additional experiment is carried out (noU$_{tot}$), where both the effects of background current and eddy current (i.e., total) are removed. The time-mean difference of CTL from noT$_e$, noU$_e$, and noU$_{tot}$ represents the effect of small-scale SST (T_e), small-scale current (U_e), and total current (U_{tot}) on wind stress, respectively. Since the evolution of mesoscale fields in the AS is strongly influenced by the internal dynamics and nonlinearities of flow field (Kindle and Thompson 1989; Vic et al. 2014), deterministic eddy-phase comparisons may not be useful. We use the eddy statistics and energetics analysis to isolate the impact of air–sea interactions via SST and surface current.
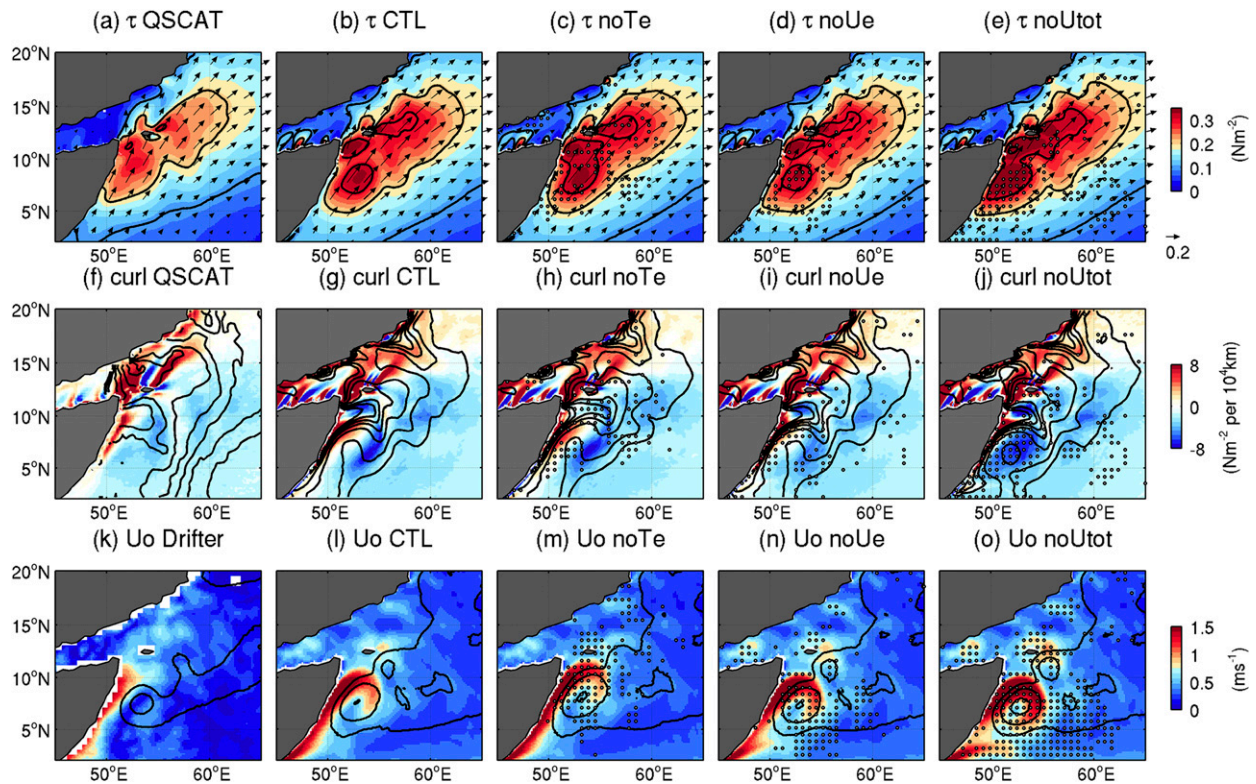
FIG. 4. The 10-yr JJAS climatologies of (top) wind stress vectors and magnitude (N m^{-2}; shading and contours, CI = 0.1), (middle) wind stress curl [N m^{-2} (10^4 km)$^{-1}$] overlaid with the SST contours (CI = 0.5°C), and (bottom) surface current speed (m s^{-1}) overlaid with the depth of 20°C isotherm Z20 (m; CI = 30, starting from 150 m). Observed wind stress and curl are estimated from the QuikSCAT, and SST and surface current speed are derived from the monthly drifter climatology data of Lumpkin and Johnson (2013). Climatologies for wind stress and curls are based on 2001–09 (9 yr), while the surface current, SST, and Z20 are based on 2001–10 (10 yr). Black dots, plotted at every 8 grid points, denote the significant difference between each sensitivity simulation and CTL at 95% confidence level.

e. Scale dependence of air–sea coupling: A 2D online smoothing

Small-scale fields during the coupled integration are filtered by an online 2D spatial smoothing (Putrasahan et al. 2013a,b; Seo et al. 2016). At every coupling interval (6 h), a 2D locally weighted scatterplot smoothing (lowess) filter (Cleveland 1979; Schlax et al. 2001) is applied to SST and/or surface currents on the 9-km ROMS grid. The bulk formula is then used to calculate the surface wind stress given the smoothed SST and/or surface current. Note that actual SST and current in ROMS remain unchanged. The spatial smoothing is made with a 5° lowess filter, which yields an effective cutoff wavelength of 3°. Small scale in this study, hence, refers to the deviation from the 3° × 3° averages. Figure 3 compares snapshots of SST and zonal/meridional surface velocities before and after the smoothing. Small-scale SSTs are mainly related to cold filamentary features along the coast of Africa and Arabia, with the CF at 10°N being the most notable mesoscale SST feature. Cold upwelled waters are advected offshore over a great distance in the form

of a zonal jet. As expected, much of small-scale SST and surface currents are removed or significantly weakened after the smoothing. However, since the SC peaks at 50 km offshore and is only 100 km wide (Düing and Schott 1978), the SC itself remains largely intact even after the smoothing. Therefore, we compare noU$_{tot}$ with CTL to infer the effect of the intense and narrow SC.

f. Observational datasets

The following observational datasets are used for model validation. The 3-daily QuikSCAT wind and wind stress are obtained from the Asia–Pacific Data-Research Center (APDRC) of the University of Hawaii on a ¼° grid from January 2001 to November 2009. The observed surface current fields are estimated from the monthly drifter climatology data of Lumpkin and Johnson (2013). The Archiving, Validation, and Interpretation of Satellite Oceanographic Data (AVISO) SSH fields on a ⅓° grid are used to detect the GW. For SST, the NOAA Optimum Interpolation (OI) ¼° SST (Reynolds et al. 2007) is used in addition to the SST climatology derived from the drifter

data. All these datasets are interpolated linearly onto the 9 km $\times$ 9 km model grid.

3. The time-mean responses in the wind and circulation fields

a. Observed and simulated climatologies

This section describes the climatologies from CTL in comparison to the observations. The differences between the model simulations are discussed in sections 3b and 3c.

Figure 4 shows the JJAS climatologies from the observed and simulated (top) wind stress vectors and magnitude, (middle) wind stress curls overlaid with SST isotherms, and (bottom) surface current speed with thermocline depth. The thermocline depth is inferred as the depth of 20°C isotherms ($Z20$). For the wind stress, the comparison to QuikSCAT is based on the 9-yr period (2001–09). Black dots denote the areas of significant changes between CTL and each of the sensitivity experiments. The observed wind stress strongly reflects the Findlater Jet along the East African coast (Findlater 1969) with peaks ($>0.2 \, \text{N m}^{-2}$) over the GW and off the Horn of Africa, penetrating offshore toward the central AS. The wind stress from CTL, while its broadscale pattern agrees well with the QuikSCAT, overestimates its intensity. However, the moored observations in the central AS (Weller et al. 2002) suggest that this overestimation is not unrealistic since the observed wind stress consistently exceeded $0.3 \, \text{N m}^{-2}$ throughout the summer of 1995 (not shown). The difference in magnitude is also likely associated with the difference in grid resolutions. Moreover, the CTL reproduces the observed maximum wind stress of up to $0.33 \, \text{N m}^{-2}$ and surface wind speed in excess of $13 \, \text{m s}^{-1}$ (now shown) over the GW (shown as $Z20$ in Fig. 4l) and its subsequent sharp decline (down to $0.23 \, \text{N m}^{-2}$ in wind stress or $11 \, \text{m s}^{-1}$ in wind speed) over the CF (shown as SST isotherms in Fig. 4g). The abrupt reduction of the wind stress over the CF disrupts continuation of the SC. Such an influence of mesoscale SST on the wind stress is suppressed in noT$_e$, the effect of which is discussed in section 3b.

In QuikSCAT and CTL, wind stress curls (Figs. 4f,g) are strongly positive in the west of the Findlater Jet axis but weakly negative over the open ocean. The negative stress curl is particularly enhanced over the eastern edge of the GW and CF. The associated negative vorticity forcing onto the ocean is known to spin up the GW (Leetmaa et al. 1982). In contrast, the positive wind stress curl tracks the northern shoulder of the GW, which abuts the southern edge of the CF. All these features are simulated reasonably well compared to QuikSCAT, although the magnitudes of wind stress curls are much stronger in the model.

The observed surface current climatology (Fig. 4k), estimated from the monthly drifter data, shows the SC has a maximum surface speed $>1.5 \, \text{m s}^{-1}$ with a width of about 100 km. Compared to this observed estimate, CTL has an overly energetic SC. However, the drifter estimate is inherently smooth (Beal et al. 2013), while the model has a higher horizontal resolution. The similar difference between the modeled and drifter-based currents is also found in Vic et al. (2014). The GW in CTL also features a deeper $Z20$ than the estimate based on the SODA climatology.

b. Effect of mesoscale SST–wind coupling

Comparison between CTL and noT$_e$ reveals time-mean rectified effect of SST–wind coupling. Since mesoscale SSTs are smoothed in noT$_e$, the wind stress exhibits less substantial mesoscale variations (Fig. 4c). That is, in noT$_e$, the Findlater Jet does not slow down over the CF and is more smoothly connected to the maximum wind stress offshore. In contrast, the wind stress over the GW remains similar in CTL and noT$_e$. This is consistent with the satellite-based study of Vecchi et al. (2004), suggesting that a significant spatial variability in the wind jet is due to oceanic mesoscale features associated with CF, which slows down the local surface winds up to $2 \, \text{m s}^{-1}$. Because of a lack of small-scale SST–wind coupling in noT$_e$, the SST-driven wind stress curl, measured as the linear relation between crosswind SST gradient and wind stress curl, is also greatly reduced in noT$_e$ (not shown). The largest difference of wind stress curl is found over the northern shoulder of the GW and CF (Fig. 4h), where the positive and negative wind stress curls become noticeably weaker in noT$_e$. That this is a result of two-way interaction between the SST gradient and wind stress curl is corroborated by the fact that the CF is weaker and narrower in noT$_e$. While the evolution of CF is driven by the internal ocean dynamics (Wirth et al. 2002), the positive wind stress curl over the southern edge of the CF, according to the conceptual model of Vecchi et al. (2004), would drive the CF southward via Ekman upwelling (Dewar and Flierl 1987). Ekman downwelling at the northern edge of CF exerts an additional forcing for the southerly position of GW and CF in CTL. Beal and Donohue (2013) observed the southward push of the GW by the intensifying cyclones (viz., CF) to occur about half of the time, suggesting that the position and shape of GW are a result of the interaction between GW and CF. This result indicates that the fine-scale SST–wind interaction plays a leading role in the southward push of the GW position.

The surface current and $Z20$ in noT$_e$ (Fig. 4m) show that the eastward jet along the eastward branch of the GW is shifted northward and that $Z20$ is slightly deeper. Since the northern edge of GW marks the SC separation
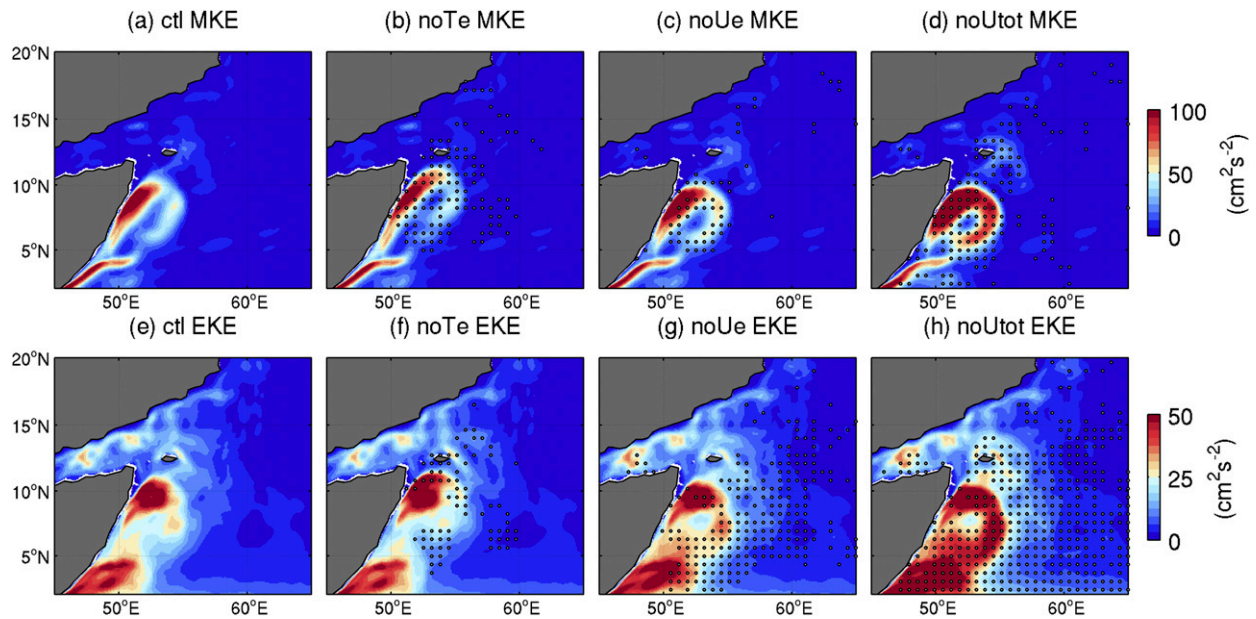
FIG. 5. The 10-yr JJAS climatologies of depth-integrated (top) MKE (cm^2 s^{-2}) and (bottom) EKE (cm^2 s^{-2}) over the western Arabian Sea. Black dots, plotted at every 8 grid points, denote the significant difference between each of the sensitivity simulations and CTL at the 95% confidence level.

from the coast (Swallow and Bruce 1966), the northeastward-extended GW in noT$_e$ would imply that the deflection of SC into the eastward jet is also shifted northeastward. Following Swallow and Bruce (1966), this study will use the location of the GW's northern shoulder to denote the latitude of SC separation. The shift in the position of the GW is further discussed in section 4.

The response in the energetics of the AS circulation due to SST–wind coupling is further illustrated in Fig. 5, which compares the mean kinetic energy (MKE) and eddy kinetic energy (EKE). Since the significant velocity associated with the SC and GW reach to 2000–3000 m deep (Swallow and Bruce 1966; Beal and Donohue 2013), the MKE and EKE are depth integrated. Nevertheless, the JJAS MKE climatology closely reflects the surface currents. Two separation points of the SC and associated peaks in EKE are found at 5° and 10°N near the Southern Gyre and GW. The MKE and EKE in noT$_e$ extend more northeastward than CTL, congruent to the northward-extended GW and CF.

Figure 6 compares locations of the SC, GW, and CF between CTL and noT$_e$. For the SC, an isotach of 1.0 m s^{-1} surface current is used. Isolines for 180-m Z20 and 15-cm SSHA denote the GW, while a 26.5°C isotherm is used for the CF. In each panel, the thin lines indicate JJAS averages of the 10 individual years indicating interannual spreads (Evans and Brown 1981), while the thick curves represent the 10-yr climatologies.

The climatologies show that the SC extends northeastward in noT$_e$ by approximately 1°. The GW also shows a northeastward-elongated pattern in noT$_e$. This altered position and shape of GW might be a result of the interaction of GW with the flanking cyclones (Jensen 1991). Indeed, Z20 shows that the Socotra Eddy is not present in noT$_e$, implying that the GW and the Socotra Eddy might have been merged and moved northward. This can be caused when the shear between the GW and the Socotra Eddy is weakened because of the weak flanking cyclones in the absence of SST-induced wind stress curl. In the observations, the merging of GW and the Socotra Eddy is observed about half of the time, and the resulting merged anticyclones move by up to 2° northward (Beal and Donohue 2013). The CF in noT$_e$ is also weaker and thinner in its meridional extent. The differences in the climatologies between the experiments tend to be greater than the standard deviation of individual experiments, suggestive of the significance of the SST–wind coupling. Note the latitudes of the SC separation from the coast are nearly the same near Bandarbeyla, Somalia, (9°N) where the slope of the continental coastline undergoes an abrupt change (Cox 1979). Therefore, the downstream extension of the SC and GW and the shrinkage of CF in noT$_e$ should be attributed to local mesoscale SST–wind interaction.

c. Effect of surface current–wind coupling

Comparing the wind stress in CTL (Fig. 4), one can see that noU$_e$ and noU$_{tot}$ display slowdown of wind
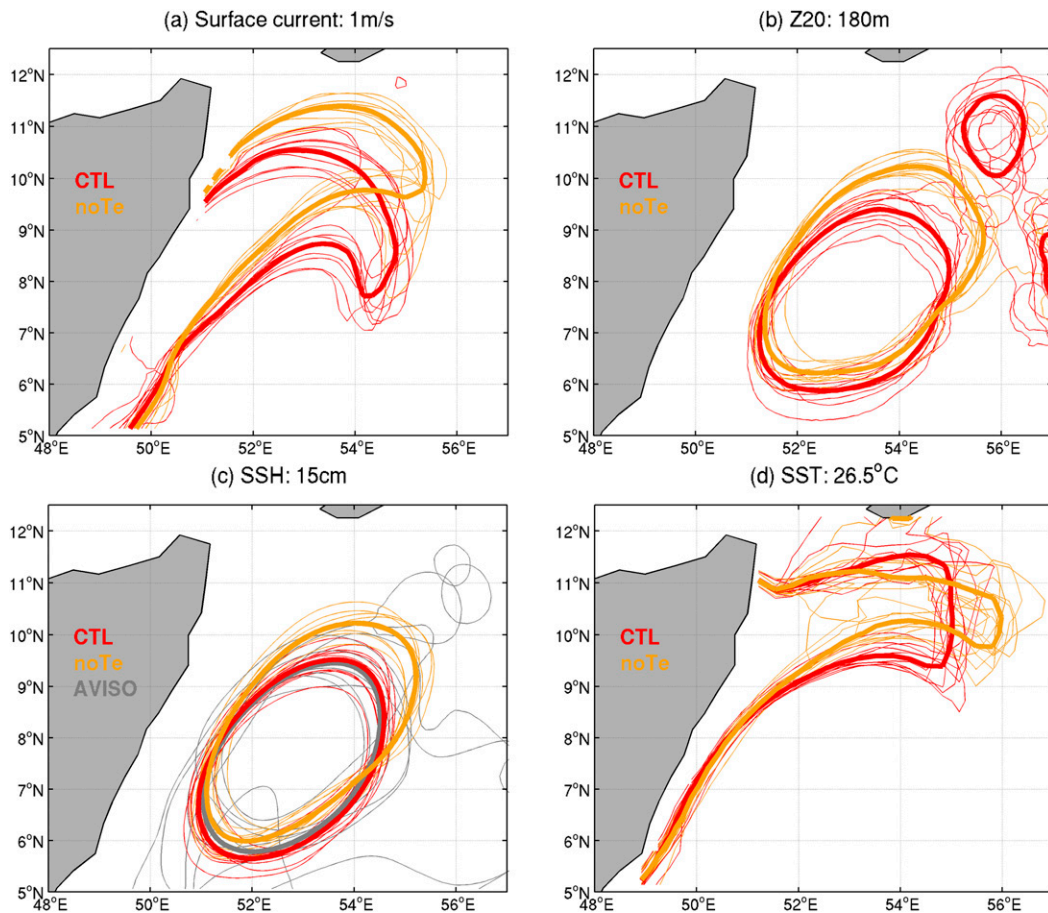
FIG. 6. (a) Comparison of the Somali Current as represented by the $1\,\mathrm{m\,s}^{-1}$ isotach for CTL (red) and noT$_e$ (yellow). Thick curves represent the 10-yr JJAS mean, while the thin curves denote the JJAS averages of individual years. (b),(c) As in (a), but for the Great Whirl shown as the 20°C isotherm Z20 and the 15-cm SSHA contours, and (d) for cold filament represented by the 26.5°C isotherms. Gray contours in (c) denote the AVISO SSHA fields.

stress over the CF. This is expected because mesoscale SST fields are not filtered. The largest difference in wind stress between noU$_e$/noU$_{tot}$ and CTL is found with its magnitude. The wind stress is significantly enhanced in noU$_{tot}$, and to a less extent in noU$_e$, which is in part because the monsoon current is oriented in the same direction as the Findlater Jet. Thus, according to (1), the ignoring the relative velocity difference yields the overestimation of the momentum flux in noU$_e$ and noU$_{tot}$ (Figs. 4n,o), resulting in enhanced MKE and EKE (Fig. 5). Despite the strengthened SC and GW, however, there is no apparent change in the position of the GW and the separation of the SC. The effect of surface current on wind stress is reflected more clearly in the stress curl. The noU$_e$ and noU$_{tot}$ show too strong negative wind stress curls over the GW compared to CTL. The anticyclonic surface vorticity over the GW is manifested as cyclonic wind stress curls, offsetting

anticyclonic curving of the wind stress (e.g., Chelton et al. 2004; Chelton 2013; Gaube et al. 2015; Seo et al. 2016). This damping effect of wind stress curl by vorticity of surface current is weakened in noU$_e$ and completely removed in noU$_{tot}$, resulting in excessive negative wind stress curl there. This coincides with too deep GWs in noU$_e$ and noU$_{tot}$, supporting the dynamical connection between enhanced negative wind stress curl and the amplified GW (Leetmaa et al. 1982).

In summary, Figs. 3–5 illustrate dynamically distinct responses of the AS circulation to SST-driven and current-driven air–sea interactions. Mesoscale SSTs create mesoscale variations in wind stress and stress curl over the energetic GW and SC, whose effect is manifested most strongly in the weaker CF, the northeastward-extended GW, and the delayed SC separation. Current–wind interaction, on the other hand, has no significant influence on the position, but instead slows down the

currents and attenuates the strength of eddies. This damping effect by the current–wind interaction appears to take place mostly on large scales (i.e., defined to be greater than the $3° \times 3°$ averages, which include the SC and much of the GW; Fig. 3), rather than on small scales, although this distinction is somewhat arbitrary, as it depends on the chosen filtering scales. The following sections look into each process in greater detail.

It is worthwhile to note that, over the southeastern part of the GW, the CTL and the QuikSCAT climatologies both exhibit a narrow and elongated band of negative wind stress curl extending southwestward along the southern limb of the GW (Figs. 4g,f). Vecchi et al. (2004) also observed this band of Ekman downwelling from their climatology (their Figs. 1 and 3), suggesting that this is because of SST–wind coupling. The comparison of wind stress curl climatologies in Fig. 4, however, implies that the enhanced and narrow negative wind stress curl there should be also more strongly attributed to current–wind coupling, in particular on the oceanic mesoscale. This is because the negative wind stress curl in noT_e (Fig. 4h) remains comparable to that in CTL but is weakened noticeably in noU_e (Fig. 4i). This negative wind stress curl appears to be enhanced when the total current effect is removed (Fig. 4j); however, this enhancement is taking place farther west over the GW as opposed to the limb of it and is due to a lack of negative surface vorticity reducing the negative wind stress curl. A careful inspection of the climatologies (Figs. 4i,j) indeed indicates that the negative wind stress curl is further reduced in noU_{tot} compared to noU_e along the thin southern limb of the GW. The relative importance of surface current compared to the SST in the negative wind stress curl in this region is expected because the SST gradient is generally weaker, being far from the influence of CF (Figs. 4f–j, contours), yet the intensity of the surface current is maintained there with the Rossby number reaching 1 (Vic et al. 2014). That Vecchi et al. (2004) observed the negative wind stress curl in this region from QuikSCAT scatterometers is perhaps because the QuikSCAT measures the wind relative to the moving ocean in addition to the SST influence on the wind.

4. Further analysis of the AS circulation responses

a. Energy sources and conversions

To further quantify causes of the modeled responses to two types of air–sea coupling, three diagnostic quantities that represent energy sources and depth-integrated energy conversions are derived from the equations of motion:

$$P = P_m + P_e$$
$$= \frac{1}{\rho_0}(\overline{u}\,\overline{\tau}_x + \overline{v}\,\overline{\tau}_y) + \frac{1}{\rho_0}(\overline{u'\tau'_x} + \overline{v'\tau'_y}), \quad (2)$$

$$C_{PE\to KE} = -\frac{g}{\rho_0}\int_{-h}^{0}(\overline{\rho}\,\overline{w} + \overline{\rho'w'})\,dz, \quad \text{and} \quad (3)$$

$$C_{MKE\to EKE} = \int_{-h}^{0} -\left(\overline{u'u'}\frac{\partial \overline{U}}{\partial x} + \overline{u'v'}\frac{\partial \overline{U}}{\partial y} + \overline{v'u'}\frac{\partial \overline{V}}{\partial x} \right.$$
$$\left. + \overline{v'v'}\frac{\partial \overline{V}}{\partial y} + \overline{+u'w'}\frac{\partial \overline{U}}{\partial z} + \overline{v'w'}\frac{\partial \overline{V}}{\partial z}\right)dz$$
$$(4)$$

Here, ρ_0 is the density of seawater, and (U, V) is the JJAS climatological velocity fields. The overbars are the time mean, and the primes are the deviation from it. Terms in (2)–(4) are integrated from the surface to the bottom of the ocean ($-h$). Equation (2) is the correlation between current and wind stress (i.e., work done by the wind on the ocean). The total wind work (P) is decomposed into mean wind work (P_m) affecting the MKE, and eddy wind work (P_e), which enters the EKE budget. If positive, wind energy is supplied to the ocean, amplifying the EKE, while, if negative, the wind slows down the mean and eddy current through friction. Equation (3) denotes the energy conversion from potential energy to kinetic energy. The term involving $\overline{\rho'w'}$ represents the eddy conversion from potential to kinetic energy, particularly important during baroclinic instability (BC). Equation (4) represents the conversion from MKE to EKE, which is dominated by two processes; the horizontal and vertical Reynolds stresses indicative of barotropic instability (BT) and vertical shear instability.

Figure 7 shows the JJAS climatologies of each of these terms calculated from CTL. The superposed contour in each subplot is an isotach of $1.0\,\mathrm{m\,s^{-1}}$ surface current, marking the location of the SC. The wind work P_m stands out as the primary energy source term, showing the maximum positive all along the SC. There is negative P_m over the eastern edge of the GW because its southward flow is against the southerly wind there. The positive P_m suggests that acceleration of the SC is a linear, scale-to-scale response to wind stress. The decomposition of P_m into P_{mx} and P_{my} confirms this scale-to-scale momentum transfer, showing that the positive P_{my} coincides with the SC, accelerating it along the coast up to 10°N. The wind work in the x direction P_{mx} takes over wind energy input to the ocean north of 8°–10°N, where the SC departs from the continental slope to flow eastward. The P_e is by an order of magnitude smaller than P_m but is comparable in size to other energy conversion processes. In CTL, P_{ex} is weakly negative over the CF because of the decline of
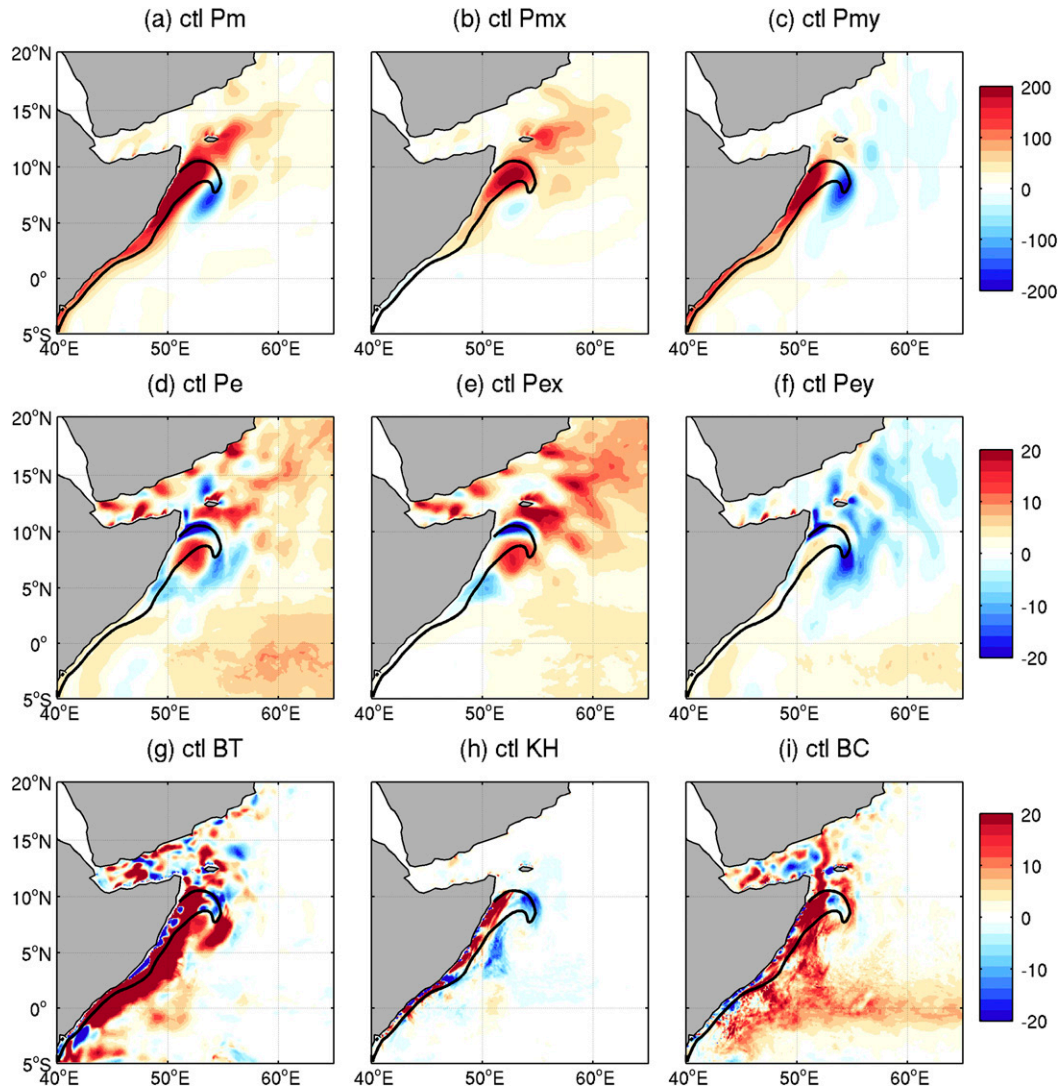
FIG. 7. Depth-integrated energy source and conversion terms ($cm^3 s^{-3}$) calculated for the JJAS 2001–10 from CTL. (a) The mean wind work P_m; (b),(c) its zonal P_{mx} and meridional P_{my} components; (d) the eddy wind work P_e; and (e),(f) its zonal P_{ex} and meridional P_{ey} components. (g)–(i) The three energy conversion processes: barotropic, vertical shear, and baroclinic instabilities. The $1 m s^{-1}$ isotach marking the approximate location and extent of the Somali Current is repeated in each panel. Note the color scale is different between (a)–(c) and (d)–(i).

wind stress there, while it is locally increased over GW as a result of enhanced wind stress over warm SST. The MKE is converted to EKE through BT, while the shear instability term is of secondary importance. BC is an important conversion process too.

b. Mesoscale SST–wind coupling

To effectively illustrate the changes in the primary energy sources and conversion processes, the two averaged profiles, color coded to denote each of the four runs, are presented in Figs. 8 and 9 (see Fig. 3h for the area of averaging). Statistically significant (95% confidence level) difference, estimated based on the two-sided Student's t test, between the sensitivity runs and CTL is denoted as filled circles. Figure 8 shows alongshore profiles as a function of latitude after averaging over 750-km distance perpendicular to the coastline. Figure 9 shows cross-shore profiles up to 750 km after averaging over 8°–11°N. Note that scales of the y axis are different. Figures 8 and 9a show that the MKE in CTL (red) peaks at around 9°N and 100 km offshore, representing the maximum large-scale energy near the GW and SC separation. The EKE (Figs. 8, 9b) shows broad offshore and alongshore distributions with peaks in 2°–4°N and 9°N near the Southern Gyre and GW. The noT$_e$ run (yellow) places the peaks in MKE and EKE slightly
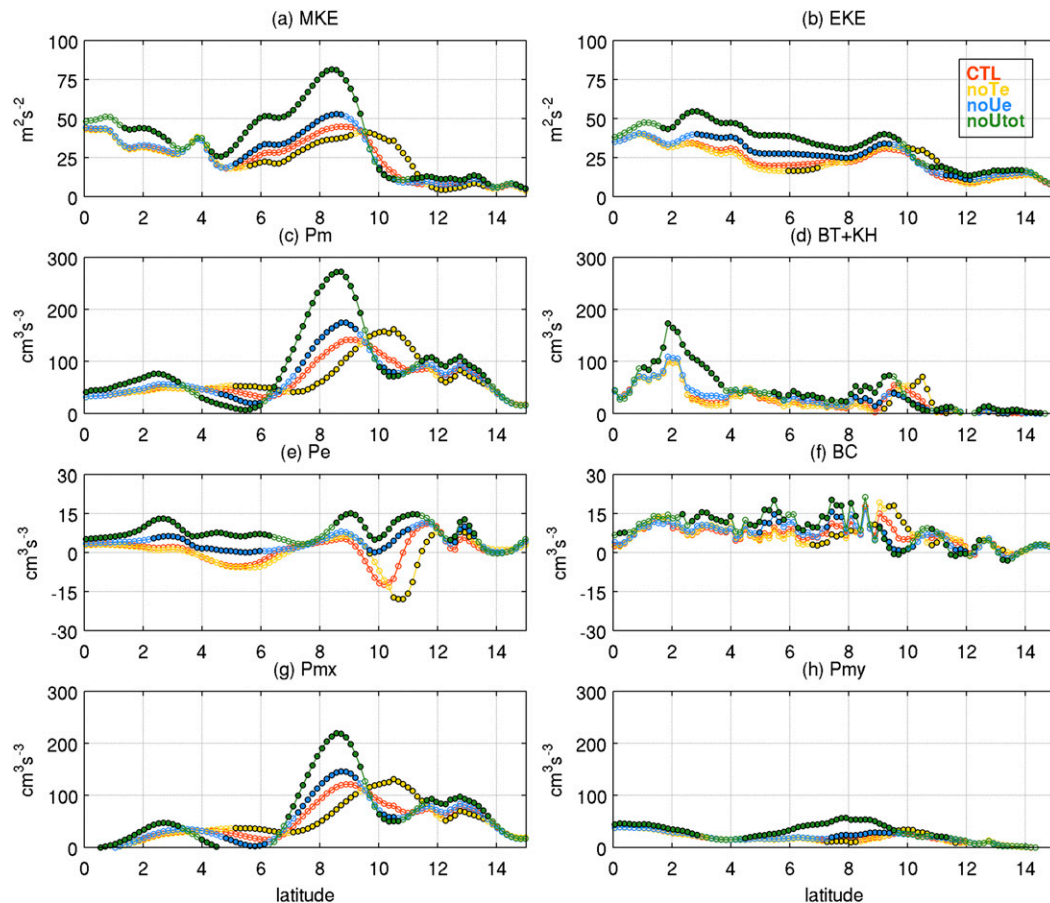
FIG. 8. Alongshore profiles as a function of latitude of the JJAS climatologies of the depth-integrated (a),(b) MKE and EKE ($m^2\,s^{-2}$) and (c)–(h) depth-integrated energy sources and conversion terms ($cm^3\,s^{-3}$) averaged over the 750-km distance perpendicular to the coastline (Fig. 3h). The filled circles in noT_e, noU_e, and noU_{tot} indicate that the difference from CTL is statistically significant at a 95% confidence level.

north of those of CTL (red), which appear with the similarly shifted peaks in P_m. This change of P_m in noT_e is almost entirely explained by that in P_{mx}, suggesting that it is the enhanced P_{mx} in noT_e that is responsible for the continuous flow of SC. In other words, in CTL the SC separation at 10°N owes its existence to the weakened P_{mx} over the CF as a result of mesoscale SST–wind coupling.

The shift in the peak of P_m results in strengthened BT (the changes in other conversion processes are relatively small), indicating that the instability process is altered near the highly sheared zone between the GW and the flanking cyclones. In noT_e, P_e is more negative and displaced northward, causing stronger dissipation of the EKE. The magnitude of P_e change is, however, much smaller than that of P_m. Therefore, the northeastward-extended GW in noT_e is attributable to higher zonal wind stress in the absence of mesoscale SST–wind coupling over the CF. Barotropic instability reinforces the eddy fields indirectly,

while the eddy-driven current–wind interaction simultaneously acts to reduce the eddy activities (Seo et al. 2016).

Figure 4 also highlighted the difference in wind stress curl climatology between CTL and noT_e. How important is the resultant Ekman pumping for the GW position and the SC separation? Figure 10 zooms into the region of the CF (denoted as the 26.5°C isotherm, solid line) and the GW (15 cm SSHA, dashed) to compare the JJAS total wind work (i.e., $P = P_m + P_e$) and Ekman pumping velocity [$W_e = (\nabla \times \tau)/(\rho f) + (\beta \tau_x)/(\rho f^2)$]; Stommel 1965]. Both CTL and noT_e show positive P in the western part of the GW and negative in the east, as expected from the anticyclonic surface flow under the southwesterly wind. The difference (CTL − noT_e) reveals enhanced P over the western part of the GW and reduced P in the center of CF. The difference in W_e is in a quadrature with that of P, with anomalous upwelling (downwelling) along the southern (northern) flank of the CF. Upwelling is weaker than downwelling; however, both reach substantial
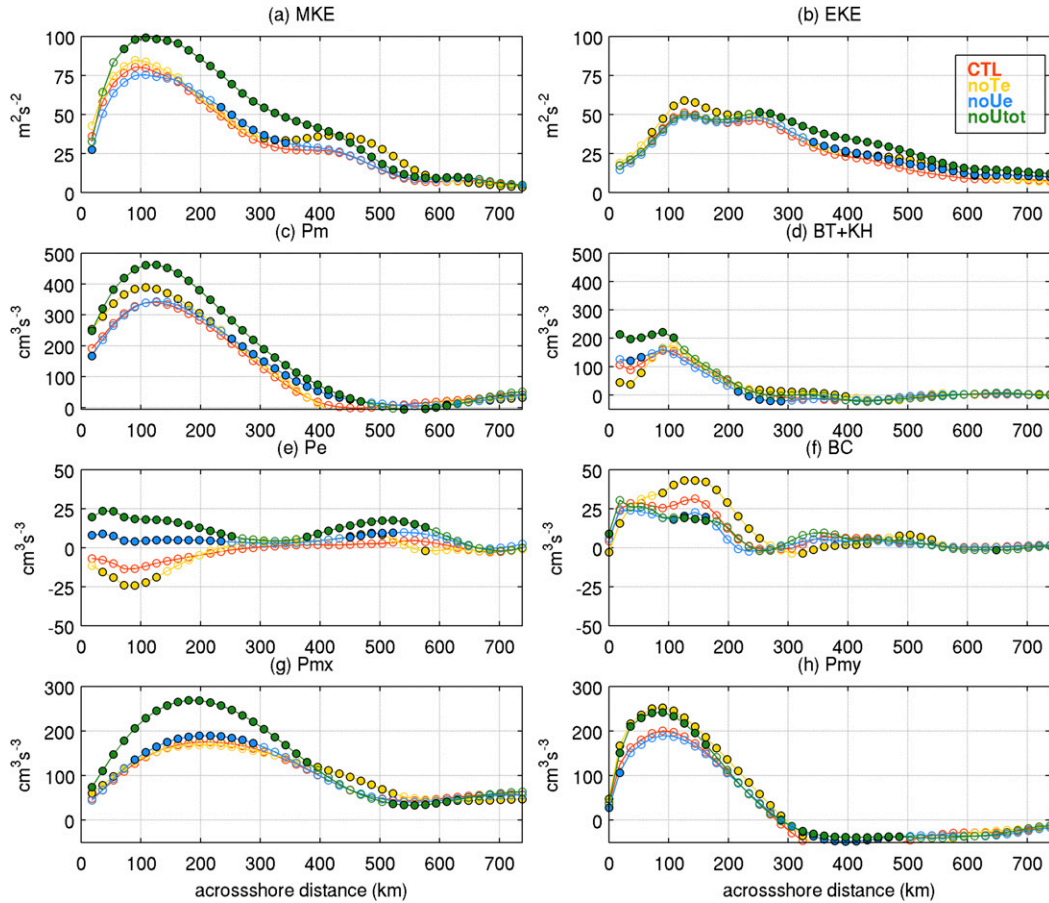
FIG. 9. As in Fig. 8, but showing the cross-shore profiles as a function of the cross-shore distance up to 750 km after averaging over 8°–11°N (Fig. 3h).

time-mean vertical motions of 2–3 m day^{-1}. There is also an elongated band of Ekman upwelling in the eastern flank of the GW because the GW in noT$_e$ is extended eastward, expanding the area of large downwelling eastward. The comparison suggests that positive (negative) W_e and P in the northern edge of the GW (CF) work in concert to maintain the GW position and SC separation.

Figure 11 confirms the shift of the GW in response to modified W_e and P and also hints at a causal relationship between the two feedback processes. It shows the time evolutions of two GW attributes, center latitude and maximum SSHA, as well as P and W_e over the GW. The GW is detected from 3-daily 15-cm SSHA closed contours (Vic et al. 2014). The GW latitude is defined as the location of maximum SSHA within the area so defined. The filled circles mark the statistically significant (95%) difference between CTL and the sensitivity simulations. This section focuses on CTL (red) and noT$_e$ (yellow). Figure 11a confirms that the GW latitude in noT$_e$ is located north of that in CTL at least by 1° (also eastward, not shown). The difference of time-mean GW latitude

remains significant throughout the period of integration. Maximum SSHA in noT$_e$ is slightly higher, especially in July–August. Thus, the analysis confirms that the GW in noT$_e$ is shifted northeastward and slightly enhanced (Figs. 4i–m). Over the GW, P in the noT$_e$ becomes greater than CTL after 15 June, reaching the largest and significant difference in July. In contrast, the difference in W_e remains insignificant until August. The timing of P and W_e, therefore, implies that the enhanced P via the SST–wind coupling energizes the GW first, while the corresponding SST anomaly induces the adjustment of W_e, further reinforcing the GW.

c. Surface current–wind coupling

Figure 4 showed that the wind stress curl in noU$_{tot}$ is significantly more anticyclonic than CTL over the GW because it lacks anticyclonic surface vorticity. This difference in wind stress curl is reflected in W_e. In contrast to CTL, W_e over the GW in noU$_{tot}$ (green) is significantly more downwelling (Fig. 11d), spinning up the GW (Fig. 11b).
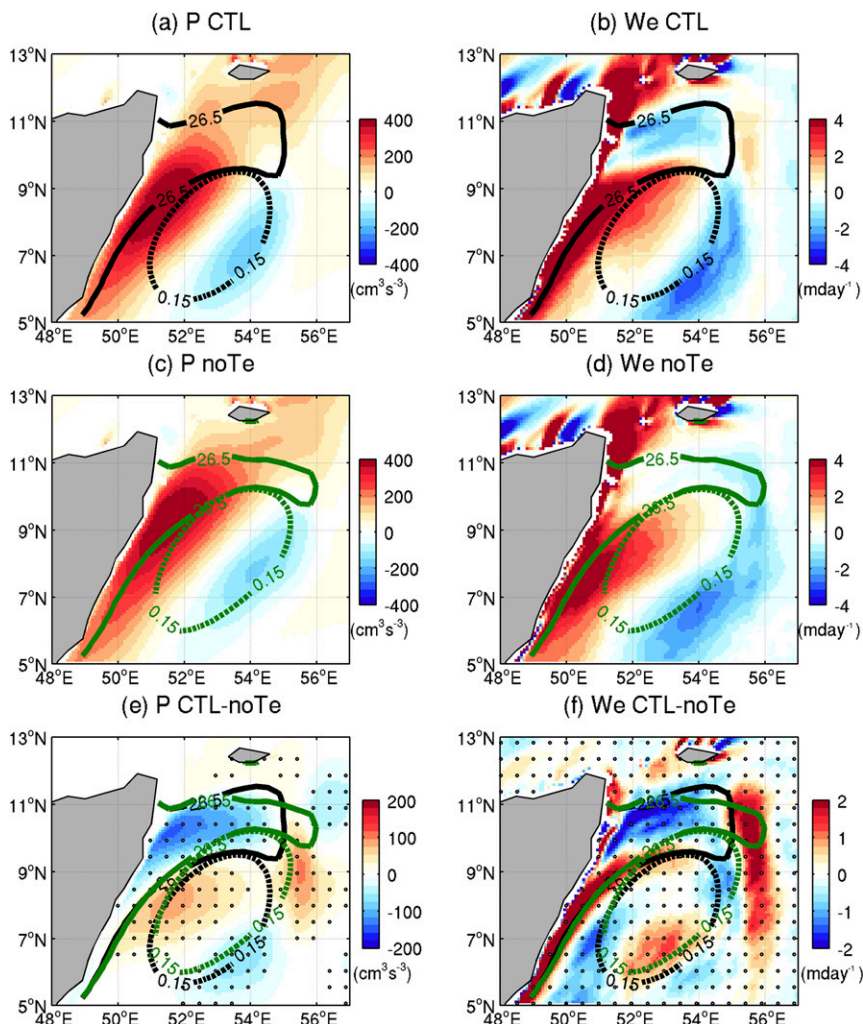
FIG. 10. (left) JJAS climatologies of the depth-integrated total wind work ($P = P_m + P_e$; cm^{3}s^{-3}) overlaid with the 26.5°C isotherm representing the approximate location and width of the cold filament (solid black for CTL and green for noT$_e$) and 15-cm isolines of SSHA denoting the GW (dashed). From (a) CTL, (c) noT$_e$, and (e) CTL- noT$_e$. (right) As in (left), but for the Ekman pumping velocity W_e (m day^{-1}; positive upward). Black dots, plotted at every 6 grid points, denote that the difference from CTL is statistically significant at the 95% confidence level.

The alongshore and cross-shore profiles (Figs. 8 and 9) show that MKE and EKE in noU$_{tot}$ (green) are significantly increased over the broad area in 5°–10°N and up to 500 km offshore (noU$_e$ to a lesser extent). When averaged, the MKE and EKE in noU$_{tot}$ are consistently higher than those in CTL by about 36% and 26%, respectively. Since the noU$_e$ shows only slightly increased MKE and EKE compared to CTL, the majority of the damping effect brought about by the current–wind interaction in CTL is deemed to originate from the large-scale currents, which includes much of the SC and GW (Fig. 3). Of course, a conclusive determination of relative importance of small scale versus large scale is

arbitrary, as it depends on the chosen filtering scale. Nonetheless, the difference between noU$_{tot}$ and noU$_e$ is substantial, highlighting the significance of the damping effect of the energetics of the ocean circulation by the surface current–wind interaction at background scale (e.g., Pacanowski 1987; Duhaut and Straub 2006; Eden and Dietze 2009).

A comparison of different energy source terms (Figs. 8 and 9) reveals that the enhanced MKE in noU$_{tot}$ is due to the increased P_m (about 29% and 38% in the cross-shore and alongshore distances, respectively). The increased P_m, in turn, arises from increased P_{mx} near the separation latitude of the SC at 9°N and up to 400 km
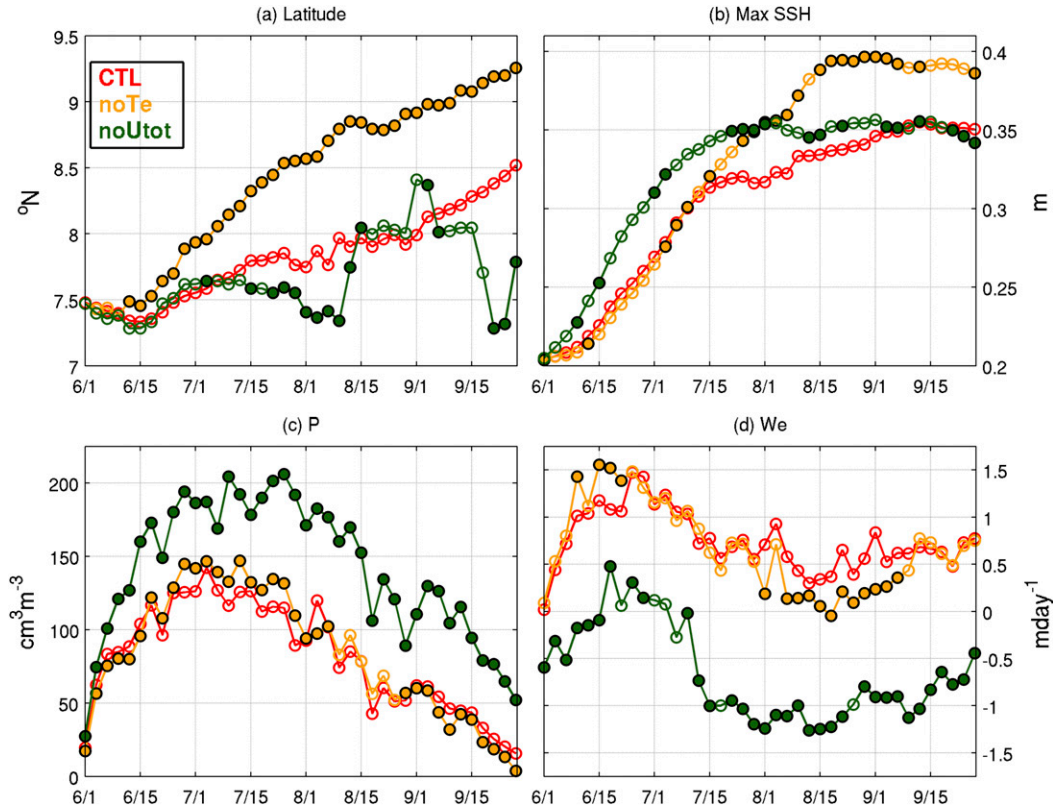
FIG. 11. Evolution of the (a) composite latitude (°N) of the GW center and (b) associated local maximum SSHA (m). (c) Wind work P (cm^3 s^{-3}) and (d) Ekman pumping velocity W_e (m day^{-1}) averaged within the composite GW. The solid lines denote the 10-yr averages, with the filled (open) circles in noTe and noUtot indicating the significant difference from CTL at the 95% confidence level.

offshore (Figs. 8g and 9g). This suggests that, in CTL, the P_{mx} is reduced over the CF and the northern branch of the GW since the eastward component of monsoonal wind is in the same direction as the eastward oceanic jet, reducing the net wind stress according to (1). The P_{my} weakly increases in noU$_{tot}$ at 6°–8°N and up to 200 km offshore, leading to the stronger SC in the absence of the relative air–sea velocity. BT is slightly increased in noU$_{tot}$ at 2° and 9°N, where the offshore jets due to the Southern Gyre and GW enhance the lateral shear. The increase in P_e is relatively small, but clearly reveals the role of eddies. The value of P_e in CTL is negative over the Southern Gyre and GW, as current–wind interaction at oceanic mesoscale dissipates the EKE through the eddy drag (Seo et al. 2016). In contrast, when this eddy-damping effect is suppressed in noU$_e$ and noU$_{tot}$, eddy current–wind interaction becomes a source, rather than a sink, of eddy energy. Thus, in noU$_{tot}$, an excess of wind work is imparted on the AS circulation, enhancing the currents. Calculation of the EKE terms suggests that increased EKE is realized through BT, while other energy conversion processes are of secondary importance. The result

from noU$_e$ tends to lie between noU$_{tot}$ and CTL, showing that small-scale ocean currents explain a small portion of the P_m increase in the AS.

5. Rectified effects on the Findlater Jet

Can these oceanic dynamical responses to air–sea interaction influence the basin-scale monsoonal winds and associated water vapor transport? To address the question of possible low-frequency rectified effect, the top two rows of Fig. 12 first show the time-mean SST and evaporation in CTL and the differences from noT$_e$ and noU$_{tot}$. The difference of CTL from noU$_e$ is similar to that from noU$_{tot}$, except with smaller magnitudes. The area of significant SST response to SST–wind coupling is limited to off the Horn of Africa because of the shift of the CF (Fig. 12b). Statistical significance of the mean response is assessed by the two-sided Student's t test at the 95% confidence level. The response in evaporation to SST–wind coupling is also concentrated near the CF but is insignificant (Fig. 12e). On the other hand, the SST response to current–wind coupling is significant on the
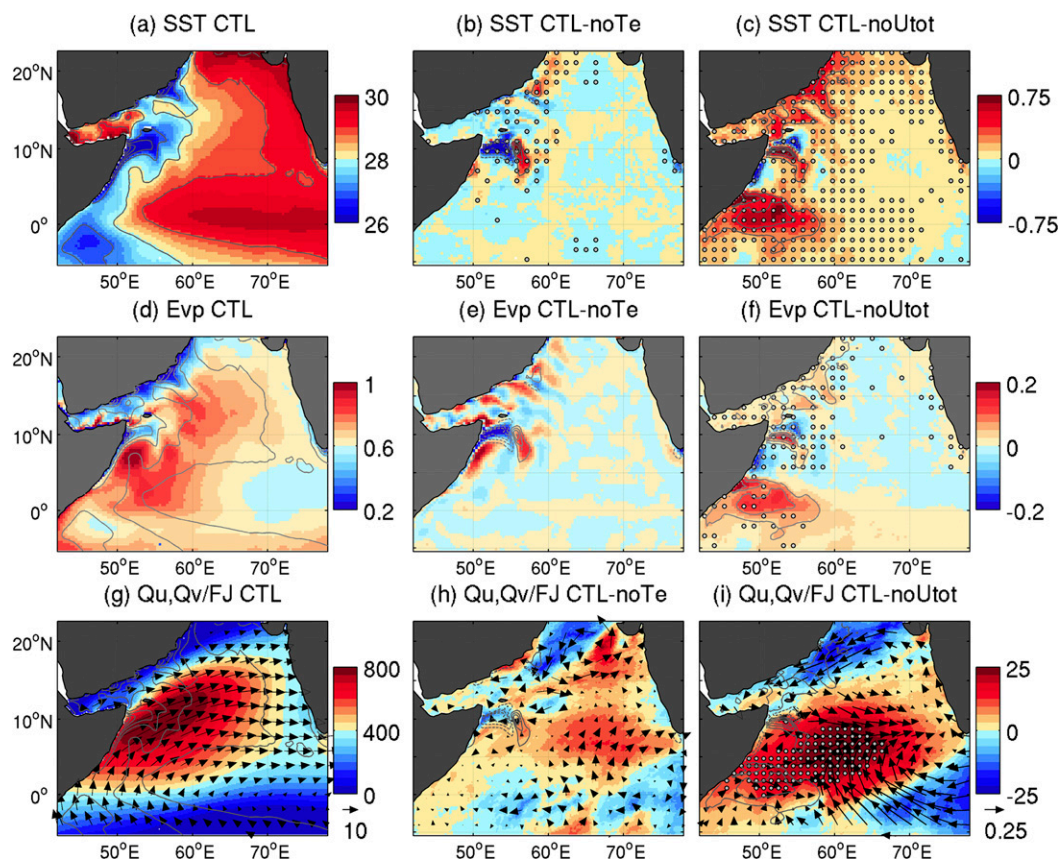
FIG. 12. The 10-yr JJAS climatologies of (a)–(c) SST (°C), (d)–(f) evaporation (Evp; cm day^{-1}), and (g)–(i) vertically integrated moisture flux transport (kg m^{-1} s^{-1}). The overlay in (a),(d),(g) is the CTL SST climatology (CI = 1); in (b),(e),(h) the overlay is the SST difference between CTL and noT$_e$ (CI = 0.25; positive solid; negative dashed; zero suppressed); and in (c),(f),(i) the overlay is the SST difference between CTL and noU$_{tot}$. The vectors in (g)–(i) denote the wind vectors at the 850-hPa level. Gray dots denote the significant response at the 95% confidence level.

broader scale (Fig. 12c), indicating a possible basin-scale adjustment of the AS monsoon system. The entire AS basin becomes warmer because of the overall weaker wind stress in CTL than noU$_{tot}$ (Fig. 4b vs Fig. 4e). The largest and most significant SST responses are found in the western basin, exceeding 1°C in association with the change in the strength of the Southern Gyre and GW. There is also an extensive warming off the Oman coast, hinting at weakened coastal upwelling. Related to the enhanced SST is the significantly increased evaporation over the Southern Gyre and GW as well as along the coast of Oman (Fig. 12f).

The changes in SST and evaporation in the western AS are of great importance to the Findlater Jet as they influence its onset and structure through the wind–evaporation feedback, which facilitates the deep tropospheric ascent and downstream intensification of the jet (Halpern and Woiceshyn 2001; Boos and Emanuel 2009). The bottom row compares changes in vertically integrated

water vapor flux transport, $(1/g)\int_{50}^{\text{sfc}}(qu + qv)\,dp$, where q is the specific humidity and (u, v) are the wind velocity. The overlaid vectors denote the wind at 850 hPa, representing the Findlater Jet (Krishnamurti and Bhalme 1976). Because of the insignificant basin-scale responses in SST and evaporation in noT$_e$, the Findlater Jet does not exhibit a significant response to SST–wind coupling, nor is there a significant shift in the moisture flux transport in the downstream (Fig. 12h). However, with current–wind coupling, the axis of the Findlater Jet has shifted slightly southeastward over the central AS (Fig. 12i). The size of the change is small compared to the mean (~5%). However, the shift of the jet yields a significant increase in water vapor flux transport directly downstream of the largest changes in SST and evaporation. The jet shift also results in the anomalous northeasterly wind along the coast of Oman, explaining reduced upwelling there.

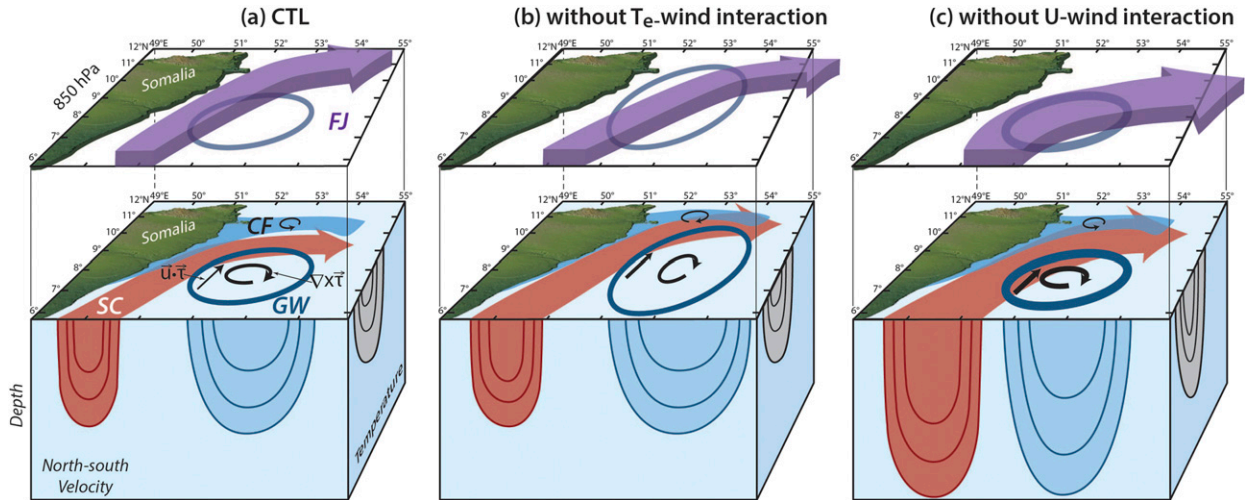It should be emphasized that our regional model domain is not broad enough to evaluate the full downstream

FIG. 13. Schematic illustrations showing the influence of SST–wind and current–wind interactions: (a) The ocean panel of the CTL shows the summertime climatology of the Somali Current (red filled arrow), Great Whirl (blue circle), and cold filament (darker blue shading). The zonal cross section depicts the northward velocity (red northward, blue southward), while the meridional cross section illustrates the isotherms. Over the GW, there is a negative wind stress curl ($\nabla \times \tau$; the arrowed circle), whereas wind work ($\mathbf{u} \cdot \tau$; black arrow) is positive over the SC and GW. Over the CF, $\nabla \times \tau$ is positive. At 850 hPa, the Findlater Jet (FJ; purple filled arrow) blows directly over the GW and CF. (b) When SST–wind coupling is suppressed, the GW is elongated northeastward by 1°, with the departure of the SC from the coast delayed to farther downstream. The width of the CF is shrunk with the anomalously negative $\nabla \times \tau$ compared to CTL. Over the western GW, $\mathbf{u} \cdot \tau$ is locally enhanced (thicker arrow). However, there is no significant change in the intensity of the SC and FJ. (c) When the current–wind coupling is suppressed, the positive $\mathbf{u} \cdot \tau$ over the SC is enhanced, which energizes the SC, so is the negative $\nabla \times \tau$ over the GW, reinforcing its strength. The positions of the SC and GW are not altered, but their strengths increase, resulting in deeper thermocline and stronger current. The FJ intensity is increased by about 5% and veers southeastward compared to that in CTL.

development of the Findlater Jet response. The sensitivity of domain size for regional model simulations has been well recognized (e.g., Seth and Giorgi 1998; Ludec and Laprise 2009). The scale of the response seen in Fig. 12i reaches that of the model domain (i.e., domain wavenumber 1), indicating that the emerging response is influenced by lateral boundary forcing data, which are identical in CTL and noU$_{tot}$. Therefore, a more robust assessment of the low-frequency rectification effect should be made with larger-scale models (Seo et al. 2009; Ratnam et al. 2009; Samson et al. 2014) or with global simulations (Izumo et al. 2008). Given the highly nonlinear nature of the Findlater Jet, the downstream atmospheric response could also be model dependent. The present analysis, nonetheless, demonstrates a potentially important influence of surface-current-driven air–sea interactions on the downstream development of monsoonal winds and moisture transport.

6. Summary and discussion

This study examined the dynamical influences of air–sea interaction mediated by the mesoscale SST and surface currents in the Arabian Sea (AS) from a series of high-resolution regional coupled model simulations. The model captures simultaneous small-scale air–sea

coupling via SST and current, while the individual effects are isolated by suppressing or removing either coupling effect. The 2D online smoothing procedure, a novel technique to separate the spatial scale of air–sea coupling via SST and surface current (Seo et al. 2016), enables identification of the effect of eddy-driven coupling from that due to large-scale coupling.

In general, the results highlight the discrete influence of air–sea interaction arising from mesoscale SST and surface current on the AS circulation. Figure 13 presents schematic illustrations that summarize the main conclusions of the study. The effect of mesoscale SST on wind stress is manifested most strongly in wind work and Ekman pumping velocity near the GW and CF, primarily affecting their positions (Fig. 13b in comparison to Fig. 13a). The maximum wind stress is found over the GW, where the SST is highest, but the wind stress over the CF 2° downstream of the GW is reduced by more than 30%. This sharp decline of the wind stress over the CF results in reduced wind work locally, leading to the offshore deflection of SC at 10°N along the northern shoulder of the GW. This scale-to-scale interaction between the ocean and the atmosphere on a relatively narrow scale is important for the modeled GW position and the SC separation in comparison to the observations. The finescale SST gradients also produce anomalous Ekman upwelling (downwelling) in the

northern edge of the GW (CF), which exerts an additional forcing of the GW and CF at the southerly position. If these SST effects are suppressed, excessive wind work over the CF allows for a continued acceleration of the SC, causing the SC and GW to extend northeastward by about 1°.

On the other hand, current–wind interaction (Fig. 13c in comparison to Fig. 13a) mostly affects the intensity of the GW and SC. The primary difference between CTL and noU$_{tot}$ is found in the amount of energy provided to the SC and GW. The MKE and EKE are significantly enhanced in noU$_{tot}$. The SC becomes evidently too fast and the GW too deep with amplified swirl velocity. Wind stress curl over the GW is too negative because of a lack of anticyclonic surface vorticity offsetting anticyclonic wind stress curl. A similar result, but with a smaller difference, is found between CTL and noU$_e$. However, the distinction between large and small scale may be arbitrary, and further studies with various filtering scales will be needed to assess the relative and respective importance robustly.

The discrete role of SST–wind and current–wind interaction in the AS is consistent with the findings by Seo et al. (2016). It was shown that SST-induced Ekman pumping affects the position of an eddy by producing a dipole of Ekman upwelling and downwelling over an eddy (Dewar and Flierl 1987). On the other hand, current-driven Ekman pumping weakens the eddy amplitudes through anomalous Ekman upwelling (downwelling) over anticyclones (cyclones) (Chelton 2013; Gaube et al. 2015). The present analysis highlights the combined importance of wind work and Ekman pumping, showing that suppressing current–wind coupling invigorates the SC and GW, while suppressing SST–wind coupling displaces them.

The study also suggests the potential downstream atmospheric influence of current–wind interaction. A noticeable shift in the Findlater Jet axis and associated column-integrated water vapor flux transport (Fig. 13c) emerge as the most striking downstream adjustment of the monsoonal circulation to air–sea interaction mediated by background surface current in the western AS. This significant downstream response in the moisture transport suggests that surface current–wind interaction in the AS is a potentially important process for simulation and prediction of the monsoon rainfall over the Indian Western Ghats (Shukla 1975; Izumo et al. 2008; Schott et al. 2009).

REFERENCES

Beal, L., and K. Donohue, 2013: The Great Whirl: Observations of its seasonal development and interannual variability. *J. Geophys. Res. Oceans*, **118**, 1–13, doi:10.1029/2012JC008198.

——, V. Hormann, R. Lumpkin, and G. Foltz, 2013: The response of the surface circulation of the Arabian Sea to monsoonal forcing. *J. Phys. Oceanogr.*, **43**, 2008–2022, doi:10.1175/JPO-D-13-033.1.

Boos, W. R., and K. A. Emanuel, 2009: Annual intensification of the Somali jet in a quasi-equilibrium framework: Observational composites. *Quart. J. Roy. Meteor. Soc.*, **135**, 319–335, doi:10.1002/qj.388.

Brandt, P., M. Dengler, A. Rubino, D. Quadfasel, and F. Schott, 2003: Intraseasonal variability in the southwestern Arabian Sea and its relation to the seasonal circulation. *Deep-Sea Res. II*, **50**, 2129–2141, doi:10.1016/S0967-0645(03)00049-3.

Carton, J. A., and B. S. Giese, 2008: A reanalysis of ocean climate using Simple Ocean Data Assimilation (SODA). *Mon. Wea. Rev.*, **136**, 2999–3017, doi:10.1175/2007MWR1978.1.

Chelton, D. B., 2013: Ocean–atmosphere coupling: Mesoscale eddy effects. *Nat. Geosci.*, **6**, 594–595, doi:10.1038/ngeo1906.

——, M. G. Schlax, M. H. Freilich, and R. F. Milliff, 2004: Satellite measurements reveal persistent small-scale features in ocean winds. *Science*, **303**, 978–983, doi:10.1126/science.1091901.

Chen, F., and J. Dudhia, 2001: Coupling an advanced land–surface/ hydrology model with the Penn State–NCAR MM5 modeling system. Part I: Model implementation and sensitivity. *Mon. Wea. Rev.*, **129**, 569–585, doi:10.1175/1520-0493(2001)129<0569: CAALSH>2.0.CO;2.

Chou, M.-D., and M. J. Suarez, 1999: A solar radiation parameterization for atmospheric studies. NASA Tech. Rep. NASA/ TM-1999–10460, Vol. 15, 38 pp. [Available online at https:// gmao.gsfc.nasa.gov/pubs/docs/Chou136.pdf.]

Cleveland, W., 1979: Robust locally weighted regression and smoothing scatterplots. *J. Amer. Stat. Assoc.*, **74**, 829–836, doi:10.1080/01621459.1979.10481038.

Cox, M. D., 1979: A numerical study of Somali Current eddies. *J. Phys. Oceanogr.*, **9**, 311–326, doi:10.1175/1520-0485(1979)009<0311: ANSOSC>2.0.CO;2.

da Silva, A. M., C. Young-Molling, and S. Levitus, 1994: *Algorithms and Procedures*. Vol. 1, *Atlas of Surface Marine Data 1994*, NOAA Atlas NESDIS 6, 83 pp.

Dewar, W., and G. Flierl, 1987: Some effects of the wind on rings. *J. Phys. Oceanogr.*, **17**, 1653–1667, doi:10.1175/ 1520-0485(1987)017<1653:SEOTWO>2.0.CO;2.

Duhaut, T. H. A., and D. N. Straub, 2006: Wind stress dependence on ocean surface velocity: Implications for mechanical energy input to ocean circulation. *J. Phys. Oceanogr.*, **36**, 202–211, doi:10.1175/JPO2842.1.

Düing, W., and F. Schott, 1978: Measurements in the source region of the Somali Current during monsoon reversal. *J. Phys. Oceanogr.*, **8**, 278–289, doi:10.1175/1520-0485(1978)008<0278:MITSRO>2.0.CO;2.

Eden, C., and H. Dietze, 2009: Effects of mesoscale eddy/wind interactions on biological new production and eddy kinetic energy. *J. Geophys. Res.*, **114**, C05023, doi:10.1029/2008JC005129.

Evans, R. H., and O. B. Brown, 1981: Propagation of thermal fronts in the Somali Current system. *Deep Sea Res.*, **28A**, 521–527, doi:10.1016/0198-0149(81)90142-4.

Fairall, C., E. F. Bradley, J. Godfrey, G. Wick, J. Edson, and G. Young, 1996: Cool-skin and warm-layer effects on sea surface temperature. *J. Geophys. Res.*, **101**, 1295–1308, doi:10.1029/95JC03190.

——, ——, J. Hare, A. Grachev, and J. Edson, 2003: Bulk parameterization of air–sea fluxes: Updates and verification for the

COARE algorithm. *J. Climate*, **16**, 571–591, doi:10.1175/1520-0442(2003)016<0571:BPOASF>2.0.CO;2.

Findlater, J., 1969: A major low-level air current near the Indian Ocean during the northern summer. *Quart. J. Roy. Meteor. Soc.*, **95**, 362–380, doi:10.1002/qj.49709540409.

Fischer, A. S., R. A. Weller, D. L. Rudnick, C. C. Eriksen, C. M. Lee, K. H. Brink, C. A. Fox, and R. R. Leben, 2002: Mesoscale eddies, coastal upwelling, and the upper-ocean heat budget in the Arabian Sea. *Deep-Sea Res. II*, **49**, 2231–2264, doi:10.1016/S0967-0645(02)00036-X.

Gaube, P., D. B. Chelton, R. M. Samelson, M. G. Schlax, and L. W. O'Neill, 2015: Satellite observations of mesoscale eddy-induced Ekman pumping. *J. Phys. Oceanogr.*, **45**, 104–132, doi:10.1175/JPO-D-14-0032.1.

Haidvogel, D. B., H. G. Arango, K. Hedstrom, A. Beckmann, P. Malanotte-Rizzoli, and A. F. Shchepetkin, 2000: Model evaluation experiments in the North Atlantic Basin: Simulations in nonlinear terrain-following coordinates. *Dyn. Atmos. Oceans*, **32**, 239–281, doi:10.1016/S0377-0265(00)00049-X.

Halpern, D., and P. M. Woiceshyn, 2001: Somali jet in the Arabian Sea, El Niño, and India rainfall. *J. Climate*, **14**, 434–441, doi:10.1175/1520-0442(2001)014<0434:SJITAS>2.0.CO;2.

Hogg, A. McC., W. K. Dewar, P. Berloff, S. Kravtsov, and D. K. Hutchinson, 2009: Effects of mesoscale ocean–atmosphere coupling on the large-scale ocean circulation. *J. Climate*, **22**, 4066–4082, doi:10.1175/2009JCLI2629.1.

Hong, S.-Y., and J.-O. Lim, 2006: The WRF single-moment 6-class microphysics scheme (WSM6). *J. Korean Meteor. Soc.*, **42**, 129–151.

——, Y. Noh, and J. Dudhia, 2006: A new vertical diffusion package with an explicit treatment of entrainment processes. *Mon. Wea. Rev.*, **134**, 2318–2341, doi:10.1175/MWR3199.1.

Hutchinson, D. K., A. M. C. Hogg, and J. R. Blundell, 2010: Southern Ocean response to relative velocity wind stress forcing. *J. Phys. Oceanogr.*, **40**, 326–339, doi:10.1175/2009JPO4240.1.

Izumo, T., C. de Boyer Montegut, J.-J. Luo, S. K. Behera, S. Masson, and T. Yamagata, 2008: The role of the western Arabian Sea upwelling in Indian monsoon rainfall variability. *J. Climate*, **21**, 5603–5623, doi:10.1175/2008JCLI2158.1.

Jensen, T. G., 1991: Modeling the seasonal undercurrents in the Somali Current system. *J. Geophys. Res.*, **96**, 22 151–22 167, doi:10.1029/91JC02383.

——, 1993: Equatorial variability and resonance in a wind-driven Indian Ocean model. *J. Geophys. Res.*, **98**, 22 533–22 552, doi:10.1029/93JC02565.

Jochum, M., and R. Murtugudde, 2005: Internal variability of Indian Ocean SST. *J. Climate*, **18**, 3726–3738, doi:10.1175/JCLI3488.1.

Kindle, J. C., and J. D. Thompson, 1989: The 26- and 50-day oscillations in the western Indian Ocean: Model results. *J. Geophys. Res.*, **94**, 4721–4736, doi:10.1029/JC094iC04p04721.

Krishnamurti, T. N., and H. N. Bhalme, 1976: Oscillations of a monsoon system. Part I. Observational aspects. *J. Atmos. Sci.*, **33**, 1937–1954, doi:10.1175/1520-0469(1976)033<1937:OOAMSP>2.0.CO;2.

Large, W. G., J. C. McWilliams, and S. C. Doney, 1994: Oceanic vertical mixing: A review and a model with a nonlocal boundary layer parameterization. *Rev. Geophys.*, **32**, 363–403, doi:10.1029/94RG01872.

Leetmaa, A., D. R. Quadfasel, and D. Wilson, 1982: Development of the flow field during the onset of the Somali Current, 1979. *J. Phys. Oceanogr.*, **12**, 1325–1342, doi:10.1175/1520-0485(1982)012<1325:DOTFFD>2.0.CO;2.

Ludec, M., and R. Laprise, 2009: Regional climate model sensitivity to domain size. *Climate Dyn.*, **32**, 833–854, doi:10.1007/s00382-008-0400-z.

Lumpkin, R., and G. C. Johnson, 2013: Global ocean surface velocities from drifters: Mean, variance, ENSO response, and seasonal cycle. *J. Geophys. Res. Oceans*, **118**, 2992–3006, doi:10.1002/jgrc.20210.

Luther, M. E., and J. J. O'Brien, 1989: Modelling the variability in the Somali Current. *Mesoscale/Synoptic Coherent Structures in Geophysical Turbulence*, J. C. J. Nihoul and B. M. Jamart, Eds., Elsevier, 373–386.

Ma, X., and Coauthors, 2016: Western boundary currents regulated by interaction between ocean eddies and the atmosphere. *Nature*, **535**, 533–537, doi:10.1038/nature18640.

Mafimbo, A. J., and C. J. C. Reason, 2010: Air–sea interaction over the upwelling region of the Somali coast. *J. Geophys. Res.*, **115**, C01001, doi:10.1029/2009JC005439.

Mahadevan, A., L. Thomas, and A. Tandon, 2008: Comment on "Eddy/wind interactions stimulate extraordinary mid-ocean plankton blooms." *Science*, **320**, 448, doi:10.1126/science.1152111.

McCreary, J. P., P. K. Kundu, and R. L. Molinari, 1993: A numerical investigation of dynamics, thermodynamics and mixed-layer processes in the Indian Ocean. *Prog. Oceanogr.*, **31**, 181–244, doi:10.1016/0079-6611(93)90002-U.

McGillicuddy, D. J., and Coauthors, 2007: Eddy/wind interactions stimulate extraordinary mid-ocean plankton blooms. *Science*, **316**, 1021–1026, doi:10.1126/science.1136256.

Mlawer, E. J., S. J. Taubman, P. D. Brown, M. J. Iacono, and S. A. Clough, 1997: Radiative transfer for inhomogeneous atmospheres: RRTM, a validated correlated-k model for the longwave. *J. Geophys. Res.*, **102**, 16 663–16 682, doi:10.1029/97JD00237.

Murtugudde, R., and A. J. Busalacchi, 1999: Interannual variability of the dynamics and thermodynamics of the tropical Indian Ocean. *J. Climate*, **12**, 2300–2326, doi:10.1175/1520-0442(1999)012<2300:IVOTDA>2.0.CO;2.

O'Neill, L. W., S. K. Esbensen, N. Thum, R. M. Samelson, and D. B. Chelton, 2010: Dynamical analysis of the boundary layer and surface wind responses to mesoscale SST perturbations. *J. Climate*, **23**, 559–581, doi:10.1175/2009JCLI2662.1.

Pacanowski, R. C., 1987: Effect of equatorial currents on surface stress. *J. Phys. Oceanogr.*, **17**, 833–838, doi:10.1175/1520-0485(1987)017<0833:EOECOS>2.0.CO;2.

Putrasahan, D., A. J. Miller, and H. Seo, 2013a: Isolating mesoscale coupled ocean–atmosphere interactions in the Kuroshio Extension region. *Dyn. Atmos. Oceans*, **63**, 60–78, doi:10.1016/j.dynatmoce.2013.04.001.

——, ——, and ——, 2013b: Regional coupled ocean–atmosphere downscaling in the Southeast Pacific: Impacts on upwelling, mesoscale air–sea fluxes, and ocean eddies. *Ocean Dyn.*, **63**, 463–488, doi:10.1007/s10236-013-0608-2.

Ratnam, J. V., F. Giorgi, A. Kaginalkar, and S. Cozzini, 2009: Simulation of the Indian monsoon using the RegCM3–ROMS regional coupled model. *Climate Dyn.*, **33**, 119–139, doi:10.1007/s00382-008-0433-3.

Renault, L., M. J. Molemaker, J. C. McWilliams, A. F. Shchepetkin, F. Lemaré, D. Chelton, S. Illig, and A. Hall, 2016a: Modulation of wind work by oceanic current interaction with the atmosphere. *J. Phys. Oceanogr.*, **46**, 1685–1704, doi:10.1175/JPO-D-15-0232.1.

——, ——, J. Gula, S. Masson, and J. C. McWilliams, 2016b: Control and stabilization of the Gulf Stream by oceanic current interaction with the atmosphere. *J. Climate*, **46**, 3439–3453, doi:10.1175/JPO-D-16-0115.1.

Reynolds, R. W., T. M. Smith, C. Liu, D. B. Chelton, K. S. Casey, and M. G. Schlax, 2007: Daily high-resolution-blended analyses for sea surface temperature. *J. Climate*, **20**, 5473–5496, doi:10.1175/2007JCLI1824.1.

Samson, G., and Coauthors, 2014: The NOW regional coupled model: Application to the tropical Indian Ocean climate and tropical cyclone activity. *J. Adv. Model. Earth Syst.*, **6**, 700–722, doi:10.1002/2014MS000324.

Schlax, M., D. B. Chelton, and M. H. Freilich, 2001: Sampling errors in wind fields constructed from single and tandem scatterometer datasets. *J. Atmos. Oceanic Technol.*, **18**, 1014–1036, doi:10.1175/1520-0426(2001)018<1014:SEIWFC>2.0.CO;2.

Schott, F. A., 1983: Monsoon response of the Somali Current and associated upwelling. *Prog. Oceanogr.*, **12**, 357–381, doi:10.1016/0079-6611(83)90014-9.

——, and D. R. Quadfasel, 1982: Variability of the Somali Current system during the onset of the southwest monsoon, 1979. *J. Phys. Oceanogr.*, **12**, 1343–1357, doi:10.1175/1520-0485(1982)012<1343:VOTSCS>2.0.CO;2.

——, and J. P. McCreary, 2001: The monsoon circulation of the Indian Ocean. *Prog. Oceanogr.*, **51**, 1–123, doi:10.1016/S0079-6611(01)00083-0.

——, S.-P. Xie, and J. P. McCreary, 2009: Indian Ocean circulation and climate variability. *Rev. Geophys.*, **47**, RG1002, doi:10.1029/2007RG000245.

Seo, H., A. J. Miller, and J. O. Roads, 2007a: The Scripps Coupled Ocean–Atmosphere Regional (SCOAR) model, with applications in the eastern Pacific sector. *J. Climate*, **20**, 381–402, doi:10.1175/JCLI4016.1.

——, M. Jochum, R. Murtugudde, A. J. Miller, and J. O. Roads, 2007b: Feedback of tropical instability wave-induced atmospheric variability onto the ocean. *J. Climate*, **20**, 5842–5855, doi:10.1175/JCLI4330.1.

——, R. Murtugudde, M. Jochum, and A. J. Miller, 2008: Modeling of mesoscale coupled ocean–atmosphere interaction and its feedback to ocean in the western Arabian Sea. *Ocean Modell.*, **25**, 120–131, doi:10.1016/j.ocemod.2008.07.003.

——, S.-P. Xie, R. Murtugudde, M. Jochum, and A. J. Miller, 2009: Seasonal effects of Indian Ocean freshwater forcing in a regional coupled model. *J. Climate*, **22**, 6577–6596, doi:10.1175/2009JCLI2990.1.

——, A. C. Subramanian, A. J. Miller, and N. R. Cavanaugh, 2014: Coupled impacts of the diurnal cycle of sea surface temperature on the Madden–Julian oscillation. *J. Climate*, **27**, 8422–8443, doi:10.1175/JCLI-D-14-00141.1.

——, A. J. Miller, and J. R. Norris, 2016: Eddy–wind interaction in the California Current System: Dynamics and impacts. *J. Phys. Oceanogr.*, **46**, 439–459, doi:10.1175/JPO-D-15-0086.1.

Seth, A., and F. Giorgi, 1998: The effects of domain choice on summer precipitation simulation and sensitivity in a regional climate model. *J. Climate*, **11**, 2698–2712, doi:10.1175/1520-0442(1998)011<2698:TEODCO>2.0.CO;2.

Shchepetkin, A. F., and J. C. McWilliams, 2005: The regional oceanic modeling system (ROMS): A split-explicit, free-surface, topography-following-coordinate oceanic model. *Ocean Modell.*, **9**, 347–404, doi:10.1016/j.ocemod.2004.08.002.

Shukla, J., 1975: Effect of Arabian Sea–surface temperature anomaly on Indian summer monsoon: A numerical experiment

with the GFDL model. *J. Atmos. Sci.*, **32**, 503–511, doi:10.1175/1520-0469(1975)032<0503:EOASST>2.0.CO;2.

Skamarock, W. C., and Coauthors, 2008: A description of the Advanced Research WRF version 3. NCAR Tech. Note NCAR/TN-475+STR, 125 pp., doi:10.5065/D68S4MVH.

Small, R. J., and Coauthors, 2008: Air–sea interaction over ocean fronts and eddies. *Dyn. Atmos. Oceans*, **45**, 274–319, doi:10.1016/j.dynatmoce.2008.01.001.

——, K. J. Richards, S.-P. Xie, P. Dutrieux, and T. Miyama, 2009: Damping of tropical instability waves caused by the action of surface currents on stress. *J. Geophys. Res.*, **114**, C04009, doi:10.1029/2008JC005147.

Stommel, H., 1965: *The Gulf Stream*. University of California Press, 248 pp.

Swallow, J. C., and J. G. Bruce, 1966: Current measurements off the Somali coast during the southwest monsoon of 1964. *Deep-Sea Res.*, **13**, 861–888, doi:10.1016/0011-7471(76)90908-6.

——, R. L. Molinari, J. G. Bruce, O. B. Brown, and R. H. Evans, 1983: Development of near-surface flow pattern and water mass distribution in the Somali Basin in response to the southwest monsoon of 1979. *J. Phys. Oceanogr.*, **13**, 1398–1415, doi:10.1175/1520-0485(1983)013<1398:DONSFP>2.0.CO;2.

Tiedtke, M., 1989: A comprehensive mass flux scheme for cumulus parameterization in large-scale models. *Mon. Wea. Rev.*, **117**, 1779–1800, doi:10.1175/1520-0493(1989)117<1779:ACMFSF>2.0.CO;2.

Vecchi, G. A., S.-P. Xie, and A. S. Fischer, 2004: Ocean–atmosphere covariability in the western Arabian Sea. *J. Climate*, **17**, 1213–1224, doi:10.1175/1520-0442(2004)017<1213:OCITWA>2.0.CO;2.

Vic, C., G. Roullet, X. Carton, and X. Capet, 2014: Mesoscale dynamics in the Arabian Sea and a focus on the Great Whirl life cycle: A numerical investigation using ROMS. *J. Geophys. Res. Oceans*, **119**, 6422–6443, doi:10.1002/2014JC009857.

Wallace, J. M., T. P. Mitchell, and C. Deser, 1989: The influence of sea surface temperature on surface wind in the eastern equatorial Pacific: Seasonal and interannual variability. *J. Climate*, **2**, 1492–1499, doi:10.1175/1520-0442(1989)002<1492:TIOSST>2.0.CO;2.

Weller, R. A., A. S. Fischer, D. L. Rudnick, C. C. Eriksen, T. D. Dickey, J. Marra, C. A. Fox, and R. R. Leben, 2002: Moored observations of upper-ocean response to the monsoon in the Arabian Sea during 1994–1995. *Deep-Sea Res.*, **49B**, 2195–2230, doi:10.1016/S0967-0645(02)00035-8.

Wirth, A., J. Willebrand, and F. Schott, 2002: Variability of the Great Whirl from observations and models. *Deep-Sea Res. II*, **49**, 1279–1295, doi:10.1016/S0967-0645(01)00165-5.

Zhai, X., and R. J. Greatbatch, 2007: Wind work in a model of the northwest Atlantic Ocean. *Geophys. Res. Lett.*, **34**, L04606, doi:10.1029/2006GL028907.

Zhang, C., Y. Wang, and K. Hamilton, 2011: Improved representation of boundary layer clouds over the southeast Pacific in ARW-WRF using a modified Tiedtke cumulus parameterization scheme. *Mon. Wea. Rev.*, **139**, 3489–3513, doi:10.1175/MWR-D-10-05091.1.